Novel Cardiac Magnetic Resonance Imaging Sequences

Used in Congenital Heart Disease

by

Serçin Özkök

A Dissertation Submitted to the

Graduate School of Sciences and Engineering

in Partial Fulfillment of the Requirements for

the Degree of

Doctor of Philosophy

in

Biomedical Engineering

KOÇ ÜNİVERSİTESİ

Date: 3 0 / 09 /2024

Novel Cardiac Magnetic Resonance Imaging Sequences

Used in Congenital Heart Disease

Koc University

Graduate School of Sciences and Engineering

This is to certify that I have examined this copy of a doctoral dissertation by

Sercin Özkök

and have found that it is complete and satisfactory in all respects, and that any and all

revisions required by the final

examining committee have been made.

Committee Members:

Prof. Kerem Pekkan (Advisor)

Prof. Özlem Yalçın

Asist. Prof. İnrahim Başar Aka

Prof. Cengizhan Örtürk

Ass. Prf. Levent Beker

With all my love, I dedicate this thesis to my beloved son, Selim İbrahim Özkök, and husband Abdullah Özkök whose time I borrowed to make these works possible.

ABSTRACT

Novel Cardiac Magnetic Resonance Imaging Sequences

Used in Congenital Heart Disease

Serçin Özkök

Doctor of Philosophy in Biomedical Engineering

September 30, 2024

Recent advancements in cardiac magnetic resonance imaging have significantly enhanced the diagnostic accuracy and management of congenital heart disease. Modern magnetic resonance imaging sequences, such as steady-state free precession, phase-contrast imaging, and late gadolinium enhancement, offer detailed anatomical and functional insights, which are crucial for precise diagnosis, surgical planning, and long-term follow-up. These sequences allow for comprehensive assessment of complex cardiac structures, hemodynamics, and myocardial tissue characterization, thereby improving patient outcomes and aiding in the effective treatment of congenital heart disease.

The integration of advanced imaging techniques like phase-contrast magnetic resonance imaging, 3D printing, and computational fluid dynamics has revolutionized the evaluation and management of congenital heart disease. Phase contrast magnetic resonance imaging provides comprehensive hemodynamic data, enabling precise assessment of blood flow patterns and quantification of flow parameters. These detailed flow analyses are further enhanced by 3D printing, which creates patient-specific models for pre-surgical planning and education. Together, these technologies offer a multifaceted approach to congenital heart disease, improving diagnostic accuracy, surgical planning, and patient-specific care.

The first part of this thesis investigates differences in functional and 3D morphological characteristics of the right ventricular outflow tract and branch pulmonary arteries in patients with surgically corrected tetralogy of Fallot, which is referred to as surgical or transcatheter pulmonary valve replacements. The study found the reduced circumferential and radial strain in the right ventricle in the surgical valve replacement group by using cardiac magnetic resonance imaging with multiplanar reconstructions, 3D volume rendering, and 3D printed models for pre-procedural assessment. A significant correlation was noted between right ventricular outflow tract types and strain parameters. This study addresses a critical gap in understanding the effects of transcatheter pulmonary valve replacement on myocardial strain in patients with surgically corrected tetralogy of Fallot.

The second part of this thesis is dedicated to determining the effects of transcatheter pulmonary valve replacement on atrial and ventricular strain in patients with surgically corrected tetralogy of Fallot using feature-tracking strain evaluation of cardiac magnetic resonance imaging. By demonstrating that pulmonary valve replacement leads to significant changes not only in volume and function parameters but also in strain characteristics it provides a deeper understanding of myocardial function in these patients. The study suggests incorporating strain analysis into routine cardiac magnetic resonance imaging protocols for a more comprehensive assessment.

ÖZET

Konjenital Kalp Hastalığında Kullanılan Güncel Kardiyak Manyetik Rezonans Görüntüleme Sekansları

Serçin Özkök

Biyomedikal Mühendisliği, Doktora

Eylül 30, 2024

Son yıllarda kardiyak manyetik rezonans görüntüleme tekniklerindeki ilerlemeler, doğuştan gelen kalp hastalıklarının tanı ve yönetimini büyük ölçüde geliştirmiştir. Modern MRI teknikleri, örneğin steady-state free precession, faz-kontrast görüntüleme ve geç gadolinyum ile kontrast kullanımı, doğru tanı, cerrahi planlama ve uzun vadeli takip için kritik olan ayrıntılı anatomik ve fonksiyonel veriler sunar. Bu yöntemler, karmaşık kalp yapılarının, hemodinamiğin ve miyokardiyal doku karakteristiklerinin kapsamlı değerlendirilmesini sağlayarak hasta sonuçlarını ve tedavi etkinliğini artırır.

Gelişmiş görüntüleme tekniklerinin entegrasyonu, faz-kontrast manyetik rezonans görüntüleme, 3D baskı ve hesaplamalı akış dinamikleri gibi, doğuştan gelen kalp hastalıklarının değerlendirilmesi ve yönetiminde devrim yaratmıştır. Faz-kontrast manyetik rezonans görüntüleme, kan akışının detaylı verilerini sağlayarak akış desenleri ve parametrelerinin hassas değerlendirilmesini mümkün kılar. Bu veriler, hasta özgü modeller oluşturan 3D baskı ile tamamlanır ve cerrahi planlama ve eğitim için kullanılır. Bu teknolojiler birlikte, tanısal doğruluğu, cerrahi planlamayı ve kişiselleştirilmiş hasta bakımını iyileştirir.

Bu tezin ilk bölümü, cerrahi olarak düzeltilmiş Fallot tetralojisi olan hastalarda sağ ventrikül çıkış yolu ve dallanan pulmoner arterlerin fonksiyonel ve 3D morfolojik özelliklerindeki farkları araştırmaktadır. Cerrahi veya transkateter pulmoner kapak replasman yapılan hastalar için multiplanar rekonstrüksiyonlar, 3D hacim renderleme ve 3D baskı modelleri kullanılarak yapılan

çalışmada, cerrahi pulmoner kapak replasman grubunda sağ ventrikülün çevresel ve radyal strain'inin azaldığı bulunmuştur. sağ ventrikül çıkış yolu tipleri ve strain parametreleri arasında anlamlı ilişkiler gözlemlenmiş olup, transkateter pulmoner kapak replasmanının miyokardiyal strain üzerindeki etkilerini anlama konusundaki önemli bir boşluğu doldurmaktadır.

Tezin ikinci bölümü, cerrahi olarak düzeltilmiş Fallot tetralojisi olan hastalarda transkateter PVR'nin atriyal ve ventriküler strain üzerindeki etkilerini özellik-takip MRI strain değerlendirmesi kullanarak incelemektedir. Çalışma, pulmoner kapak replasmanının sadece hacim ve fonksiyon parametrelerinde değil, aynı zamanda strain özelliklerinde de önemli değişikliklere yol açtığını vurgulayarak miyokardiyal fonksiyon hakkında daha derin bir anlayış sunmaktadır. Strain analizinin rutin kardiyak MRI protokollerine dahil edilmesinin, kalp sağlığının daha kapsamlı bir değerlendirmesini sunabileceği önerilmektedir.

ACKNOWLEDGEMENTS

I would like to extend my deepest gratitude to my advisor, Prof. Kerem Pekkan, for his unwavering support throughout my PhD. His patience and guidance during challenging times were invaluable, and it was truly a privilege to work under his mentorship.

I am also grateful to my thesis committee members, Prof. Özlem Yalçın and Dr. İbrahim Başar Aka, as well as Prof. Cengizhan Öztürk, and Dr. Levent Beker for serving on my defense jury.

Thanks to my colleagues Tansu Gölcez, Berk Ural, and Eda Nur Saruhan in Pekkan's lab for their friendship and the enjoyable moments we shared during my studies. Special thanks to Dr. Kevser Banu Köse for her warm help and pure friendship at every moment of research discussions.

Finally, I owe my deepest thanks to my husband and my parents, whose love and encouragement have always been my greatest motivation.

TABLE OF CONTENTS

Page

List of Tables

List of Figures

Figure 4.1: Computational fluid dynamics simulations of (A, D) pre-surgery, (B, E) selected surgical alternative, and (C, F) post-surgery model. The first row shows the streamlines of inflows in different colors (A–C). The hepatic flow split is shown in red color. The second row indicates the velocity streamlines and total venous flow splits to the lungs (D–F). Quantified flow splits to the lungs are reported in percentages.

Abbreviations

AZY	Azygos Vein
CFD	Computational Fluid Dynamics
CHD	Congenital Heart Disease
HEP	Hepatic Vein
IVC	Inferior Vena Cava
LPA	Left Pulmonary Artery
MPA	Main Pulmonary Artery
MRA	Magnetic Resonance Angiography
MRI	Magnetic Resonance Imaging
PA	Pulmonary Arteries
PR	Pulmonary Regurgitation
RPA	Right Pulmonary Artery
PVR	Pulmonary Valve Replacement
RVOT	Right Ventricle Outflow Tract
RPA	Right Pulmonary Artery
SVC	Superior Vena Cava
TOF	Tetralogy of Fallot
TCPC	Total Cavopulmonary Connection

Chapter 1

1 INTRODUCTION

The prevalence of congenital heart disease (CHD) is approximately 1 in 100 live births, and advancements in surgical techniques and medical management have significantly improved survival rates, with around 90% of affected individuals reaching adulthood (Pushparajah, K et al. 2019). With the recent advances in sequence techniques, magnetic resonance imaging (MRI) had an essential role in the diagnosis and management of congenital heart disease (CHD). It provides high spatial and temporal resolution with detailed anatomical and functional information that is critical for the comprehensive evaluation of CHD without ionizing radiation, making it especially valuable in pediatric populations and for long-term follow-up (Luijten LW et al. 2015). Cardiac magnetic MRI is widely accepted as the gold standard imaging technique for assessing cardiac morphology, measuring biventricular volume and function, and quantifying hemodynamic parameters such as flow and pressure across valves and shunts. And also providing detailed information about non-invasive myocardial tissue characterization. (Buechel et al. 2015).

One of the crucial cardiac MRI techniques that has significantly advanced the assessment of CHD is phase-contrast imaging, which allows for quantifying blood flow dynamics and evaluating shunts and valvular function (Buechel et al. 2015). 2D phase-contrast cardiac MRI has been used routinely in the clinical setting for assessing valvular and vascular disease in pediatric CHD patients. This technique involves the acquisition of a single slice perpendicular to the vessel of interest, allowing for the measurement of blood flow velocity and volume at that location (Buechel et al. 2015). It has been especially useful in assessing valvular regurgitation, stenosis, and shunt quantification (Fratz et al. 2013). Among the novel sequences, phase-contrast imaging stands out for its ability to quantify blood flow dynamics, allowing for precise assessment of shunts and valvular function (Buechel et al. 2015). This technique is invaluable in both pre-operative planning and post-operative follow-up, as it provides essential data on hemodynamics that can influence clinical decisions.

However, 2D phase-contrast cardiac MRI is limited by its inability to capture complex, three-dimensional flow patterns and the need for multiple breath-holds or free-breathing acquisitions to cover the entire heart and great vessels. To overcome these limitations, 4D flow cardiac MRI has emerged as a powerful tool for comprehensively evaluating cardiovascular hemodynamics in CHD. 4D flow cardiac MRI acquires time-resolved, three-dimensional datasets with velocity encoding in all three spatial directions, allowing for the quantification of blood flow
throughout the entire cardiac cycle (Kilner et al. 2010). This technique provides a wealth of information, including flow volumes, velocities, and derived parameters such as wall shear stress and turbulent kinetic energy, which can be used to assess the severity of valvular lesions, detect shunts, and identify areas of abnormal flow patterns (Ginat et al. 2011). It provides the ability to retrospectively analyze flow in any plane or vessel of interest without the need for precise planning of 2D slice locations (Dillman et al. 2013).

Contrast-enhanced magnetic resonance angiography (MRA) is another essential imaging sequence particularly effective in delineating complex vascular anatomy, allowing for identifying anomalies such as stenosis, shunts, and collateral vessels. The development of time-resolved 3D MRA allows for the visualization of dynamic blood flow patterns, providing insights into hemodynamics that are critical for evaluating the severity of lesions and planning interventions (Kilner et al. 2010).

Integrating MRA with 3D modeling and printing techniques enhances the utility of this imaging modality. Three-dimensional reconstructions from MRA data allow for detailed visualization of the heart and great vessels, facilitating a better understanding of complex anatomical relationships (Ginat et al. 2011). These models can be utilized for pre-operative simulations and training (Ma et al. 2015) to improve communication among the surgical team, patients, and their families. The models have the potential to personalize surgical approaches, ultimately leading to improved patient outcomes and reduced operative times (Valverde et al. 2017). The process of creating 3D-printed models from MRA data involves several steps, including image acquisition, post-processing, and segmentation. Advanced software tools allow for the conversion of MRA images into 3D printable formats, enabling the production of accurate physical models that can be used not only to enhance the understanding of complex cardiac anatomy but also pre-operative simulations and training, improve patient education and cooperation (Ma et al. 2015).

Cardiac MRI provides the necessary anatomical and flow data to construct patient-specific computational fluid dynamics (CFD) models. Contrast-enhanced MRA allows for high-resolution 3D visualization of vascular structures, which can be segmented and converted into computational meshes (Ginat et al. 2011). Time-resolved 2D or 4D phase-contrast MRI sequences provide quantitative measurements of blood flow velocities and volumes throughout the cardiac cycle, which can be used as boundary conditions for CFD simulations (Markl et al. 2016). By integrating these MRI-derived data into computational models, it becomes possible to calculate detailed hemodynamic parameters such as pressure gradients, wall shear stress, and flow patterns that would be challenging to measure invasively. One of the significant advantages of MRI-based CFD is its ability to predict hemodynamic changes resulting from different surgical interventions. For instance, in patients with aortic coarctation, CFD has been shown to correlate well with invasive pressure measurements, providing a reliable alternative to catheterization (Goubergrits et al. 2015). Furthermore, CFD simulations can evaluate the impact of various surgical strategies on blood flow dynamics, thereby optimizing treatment plans tailored to individual patient anatomies (Liu et al. 2018).

This thesis is divided into two main parts. The first part of this thesis, which consists of two chapters (Chapter 2 and 3), is dedicated to the in vivo detection of myocardial distortion and the relationship between right ventricle outflow tract (RVOT) morphology of repaired tetralogy of Fallot (TOF) before and after pulmonary valve replacement (PVR).

In chapter 2, the morphology of the right ventricular outflow tract and the cardiac MRI characteristics in patients who underwent surgical and transcatheter PVR after TOF repair are evaluated to differentiate the MRI characteristics between surgical and transcatheter PVR. Biventricular volume, function, and blood flow analyses were assessed in detail. Morphological features of the RVOT were classified into five different types: trapezoid, tubular, inverted trapezoid, apple, and hourglass, using 3D-segmented models. Myocardial distortion is also evaluated in terms of circumferential and radial strain. Morphological and mechanical characteristics were compared between sıurgical and transcatheter PVR groups. It was concluded that pre-procedural MRI strain, right-to-left pulmonary artery flow, diameter ratio, and RVOT morphological features play a crucial role in selecting the appropriate PVR method. The strain characteristics (circumferential and radial) of the right ventricle were worse in the surgical group. It was concluded that there was a significant relationship between RVOT morphology and right ventricular end-diastolic volume index, as well as global circumferential and radial MRI strain.

In Chapter 3, the impact of transcatheter PVR on atrial and ventricular myocardial distortion in patients with repaired TOF using feature-tracking cardiac MRI was evaluated. In terms of myocardial distortion of both atrial reservoir, conduit, and pump strains were evaluated. Specifically, left and right atrial conduit and pump strains increased, indicating enhanced myocardial function. The global circumferential, longitudinal, and radial strains of the left ventricle, as well as the right ventricular global circumferential strain, also showed significant improvement. Despite these positive changes, the right ventricular longitudinal and radial strains remained unchanged. The study underscores the efficacy of feature-tracking cardiac MRI in assessing myocardial strain and suggests that tPVR positively influences myocardial function, although some strain parameters, particularly in the right ventricle, may still be affected by pre-existing damage and surgical history.

In Chapter 4, the second part of the thesis, pulmonary flow distribution in patients with single-ventricle physiology after Fontan surgery is assessed through patient-specific surgical modeling was evaluated. This chapter involves simulating blood flow using computational experiments, emphasizing the crucial role of balanced hepatic flow to both lungs for better long-term outcomes. The research demonstrates that by tailoring surgical techniques to each patient's unique anatomical features, it is possible to achieve a more even distribution of hepatic flow, potentially mitigating the severe complications frequently observed in these patients.

Chapter 2

2 MORPHOLOGIC DIFFERENCES OF RIGHT VENTRICULAR OUTFLOW TRACT IN PATIENTS WITH REPAIRED TETRALOGY OF FALLOT REFERRED TO SURGICAL OR TRANSCATHETER PULMONARY VALVE REPLACEMENT

2.1 Introduction

Tetralogy of Fallot (TOF) is the most common cyanotic congenital heart disease. It consists of right ventricular hypertrophy, ventricular septal defect, and right ventricular outflow tract (RVOT) obstruction (Meca Aguirrezabalaga JA et al. 2020). The primary surgical approach aims to relieve RVOT narrowing and closure of the left-to-right shunt. The severity of pulmonary stenosis and the anatomy of RVOT determine the surgical approach, which varies from RVOT muscle bundle resection or a pulmonary valve-sparing approach to the right ventricle to pulmonary artery conduit (Meca Aguirrezabalaga JA et al. 2020). Increasing numbers of patients with repaired TOF reach adulthood due to recent advances in surgical techniques and medical follow-up. However, the initial surgical correction may result in residual pulmonary regurgitation (PR) associated with right ventricle dilatation, dysfunction, and adverse clinical outcomes (Meca Aguirrezabalaga JA et al. 2020). The increased patient population with PR has strengthened the importance of the PVR in managing long-term morbidity and mortality (Therrien J et al. 2005; Stout KK et al. 2019).

Pulmonary valve replacement (PVR) is recommended by European and American Guidelines in symptomatic patients with pulmonary regurgitation and/or right ventricular outflow stenosis to restore pulmonary valve function while improving cardiac function with pulmonary regurgitation and/or right ventricular outflow stenosis to restore pulmonary valve function while improving cardiac function (Stout KK et al. 2019; Baumgartner H et al. 2021). Transcatheter and surgical pulmonary valve replacements have the same indications based on findings from cardiac magnetic resonance imaging (MRI) and clinical features.

PVR can be performed using two techniques: surgical or transcatheter. Surgical PVR is accepted as a gold-standard technique for PR and is indicated in patients with large RVOT, positive coronary compression during balloon sizing, or coronary anomalies (Boshoff DE et al. 2013). However, the invasive nature requiring a sternotomy is the main limitation of the technique. Since the last two decades, transcatheter PVR has been used as an alternative technique to surgical PVR in selected patients with the right ventricle-to-pulmonary artery conduits, bioprosthetic valves, and native RVOT in suitable anatomy (Gillespie MJ et al. 2012). Transcatheter PVR is not recommended in large native RVOT (>28 mm) and small conduits (<16mm) (Boshoff DE et al. 2013). The main limitation in clinical practice is that the transcatheter PVR and surgical PVR are mentioned under the same indications, and there is no definite indication for surgical vs. transcatheter PVR yet. The other limitation in clinical practice is the impact of PVR on long-term adverse clinical outcomes, and reverse atrial and ventricular remodeling is still scarce and controversial (Ferraz Cavalcanti PE et al. 2013; Van den Eynde J et al. 2022).

In this chapter, the effects of PVR on cardiac function and morphology by analyzing cardiac MRI characteristics were comprehensively evaluated. This includes comparing MRI strain, branch pulmonary artery flow distribution, and the morphological features of the right ventricular outflow tract and branch pulmonary arteries between surgical and transcatheter replacement methods. Additionally, we sought to understand atrial and ventricular reverse remodeling post-procedure using feature-tracking strain techniques to potentially enhance the indications and outcomes of pulmonary valve replacement.

2.2 Materials and Methods

2.2.1 Patient groups and data collection

Preprocedural cardiac MRI of 166 patients with repaired TOF were reviewed. All cardiac MRIs were performed to evaluate the need for pulmonary valve replacement. Among these, patients who have been undergoing PVR were included in the study. A total of 36 patients who underwent surgical (28 patients) or transcatheter (8 patients) PVR were included. All the patients had the same history of ventricular septal defect closure and right ventricular outflow tract patch augmentation in surgical history. The patients with a right ventricle-to-pulmonary artery conduit who already had valve-in-valve implants or controlled cardiac MRIs were not included. The flow chart of the inclusion and exclusion criteria is presented in **Figure 2.1**.

The demographic data (sex, age) and clinical information were retrieved from the hospital database. The type of surgical procedures, echocardiography, electrocardiography, and cardiac catheterization findings were recorded. The weight and height of the patients were also recorded before the examination to calculate body surface area.

The decision to perform PVR was established according to the indications for either surgical or transcatheter PVR as moderate-to-severe pulmonary regurgitation higher than 25% on cardiac MRI and at least two of the following criteria in asymptomatic patients:

- right ventricle end-diastolic volume index higher than 150 mL/m2,
- right ventricle end-systolic volume index higher than 80 mL/m2,
- right ventricle ejection fraction less than 47%,
- severe branch pulmonary artery stenosis (blood flow less than 30% to affected lung)
- QRS duration longer than 160 ms on the electrocardiogram (Geva T 2013).

In addition, patients with favorable anatomy and pulmonary valve annulus <30 mm by cardiac MRI received transcatheter PVR and patients with right-to-left flow ratio higher than 1.5, and severe aortic regurgitation received surgical PVR.

Cardiac catheterization was performed to evaluate the patient's eligibility for transcatheter pulmonary valve replacement. A positive coronary compression test, severe aortic regurgitation, the need for concomitant surgical correction, and a large aneurysmal right ventricle outflow tract prompted the decision for surgical pulmonary valve replacement.

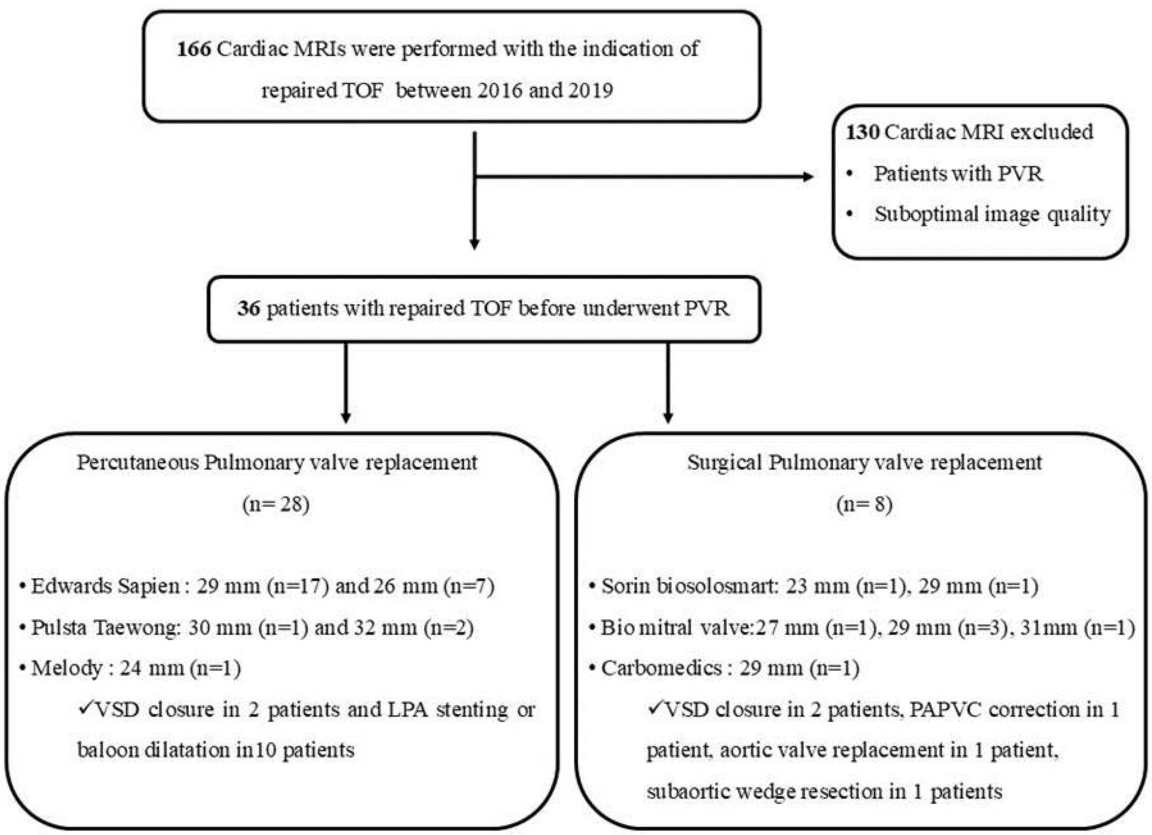

Figure 2. 1: Flow chart showing the patient selection with inclusion and exclusion criteria. The characteristics of transcatheter and surgical pulmonary valve replacement groups are also shown.

2.2.2 *Cardiac magnetic resonance imaging technique*

Cardiac MRI examinations were performed using a 1.5-tesla (T) MRI scanner (450W; GE Medical Systems, Waukesha, WI) with a 32-channel phased-array abdominal coil. All examinations were performed without sedation. T2-weighted non-ECG gated fast imaging employing steady-state acquisition sequence in the axial, coronal, and sagittal planes through thorax were revealed to guide the cardiac MRI planes. Applied typical parameters were as follows: repetition time/echo time [TR/TE] 3/1 ms; flip angle 60°; bandwidth ±111 kHz; matrix 224×224; field-of-view 350 mm; the number of excitations 1; slice thickness7 mm; gap 1.5 mm.

Cine steady-state free precession sequence was performed in two-chamber, four-chamber, short axis, and right ventricular outflow tract planes of the heart to assess ventricular volume and function. Applied parameters were as follows: TR 3.6 ms; TE 1.5 ms; flip-angle 60°; bandwidth ± 90 kHz; matrix 192×192; FOV 350 mm; NEX 1; slice thickness 8 mm; gap 0 mm.

A 0.2 mmol/kg gadolinium-based contrast agent was used during MRA to assess the vascular anatomy and to guide the phase-contrast images of the pulmonary arteries. Time-resolved imaging of contrast kinetics (TRICKS) sequence was used for magnetic resonance angiography (MRA), and applied parameters on the coronal plane were as follows: TR 4.2 ms; TE 1.4-11 ms; flip-angle 30°; bandwidth ± 50 kHz; matrix 320x192; FOV 350 mm; NEX 1; slice thickness 8 mm; gap 0 mm.

Phase-contrast imaging sequence was performed to assess the blood flow of the main pulmonary artery (MPA), left pulmonary artery (LPA), right pulmonary artery (RPA), and ascending aorta perpendicular to the vascular structures in a double-oblique plane on multiplanar reconstructed images of magnetic resonance angiography to minimize measurement errors. The optimal velocity encoding value of the pulmonary artery was calculated by using the doppler velocity according to the Bernoulli equation (Oshinski JN et al. 1996). The velocity was increased by 50 cm/s until there was no aliasing artifact. Applied parameters for the phase contrast imaging sequence were as follows: TR 5 ms; TE 3 ms; flip-angle20°; bandwidth ± 60 kHz; matrix 192×160; FOV 350 mm; NEX 1; slice thickness 8 mm; gap 0 mm. Each set of images was acquired with retrospective ECG gating and 20 reconstructed cardiac phases. The images were acquired during 13 ±3 seconds breath-hold duration depending on the heart rate during the end-expiratory breath-hold. The duration of the examination changes between 45 to 65 seconds. Cardiac MRI protocol used in congenital heart disease and imaging parameters are demonstrated in **Table 2.1.**

Table 2. 1: Cardiac MRI examination protocol and scan parameters used in the patient with congenital heart disease and repaired tetralogy of Fallot

	MRI SEQUENCE	**PLANE**	**SEQUENCE PARAMETERS**
LOCALISER	FIESTA (Non-cardiac gated)	Axial-coronal-sagittal plane	TR 3 ms; TE 1 ms; flip-angle 60°; bandwidth ± 111 kHz; matrix 224×224; FOV 350 mm; NEX 1; slice thickness 8 mm; gap 2 mm.
FUNCTIONAL EVALUATION	Cine - FIESTA (Cardiac gated)	Two chamber view Four chamber view Short axis view RVOT- view	TR 3.6ms; TE 1.5ms; flip-angle 60°; bandwidth ± 90 kHz; matrix 192×192; FOV 350 mm; NEX 1; slice thickness 8 mm; gap 0 mm.
BLOOD FLOW ASSESSMENT	Phase-contrast imaging	Ascendan aorta Descendan aorta Main pulmonary artery, Left and right pulmonary artery	TR 5 ms; TE 3 ms; flip-angle20°; bandwidth ± 60 kHz; matrix 192×160; FOV 350mm; NEX 1; slice thickness 8 mm; gap 0 mm.
MRA	TRICKS/TWIST-Time-Resolved MR Angiography	Coronal	TR 4.2 ms; TE 1.4-11 ms; flip-angle 30°; bandwidth±50 kHz; matrix 320x192; FOV 350 mm; NEX 1; slice thickness 8 mm; gap 0 mm.

2.2.3 Cardiac magnetic resonance imaging evaluation

Biventricular volume and function, blood flow analyses, and MRA were analyzed using a commercially available software program (5.6i report card, GE Medical Systems, Milwaukee, WI) and a workstation (Advantage Workstation, GE Medical Systems, Waukesha, WI). The function and the volume of both ventricles were measured by contouring the endocardial layer of the ventricles manually by including papillary muscles and the trabeculations on short-axis cine images for both end-diastolic and end-systolic phases. Body surface area (with Mosteller's formula), biventricular end-diastolic volume index, end-systolic volume index, stroke volume index, ejection fraction, and strain data were calculated automatically and recorded. For the flow analysis, the contour of the vascular structures was traced manually. Pulmonary regurgitation fraction (RF) was calculated automatically. However, the percentage of the blood flow distribution of branch pulmonary arteries was calculated manually. The formula is net LPA or RPA flow volume/ sum of both pulmonary arteries flow volume x 100 in %.

A multiplanar reconstructed image of MRA perpendicular to the long axis in the pulmonary phase was used to measure the RVOT and pulmonary arteries in exact diameter. Two diameters perpendicular to each other were averaged and converted to a z-score. RVOT was measured at four points as subvalvular RVOT, approximate pulmonary valve annulus, supravalvular, and proximal to bifurcation. The size of the branch pulmonary arteries was also measured at the narrowest diameter. The measurement of RVOT in MRA is shown in **Figure 2.2.**

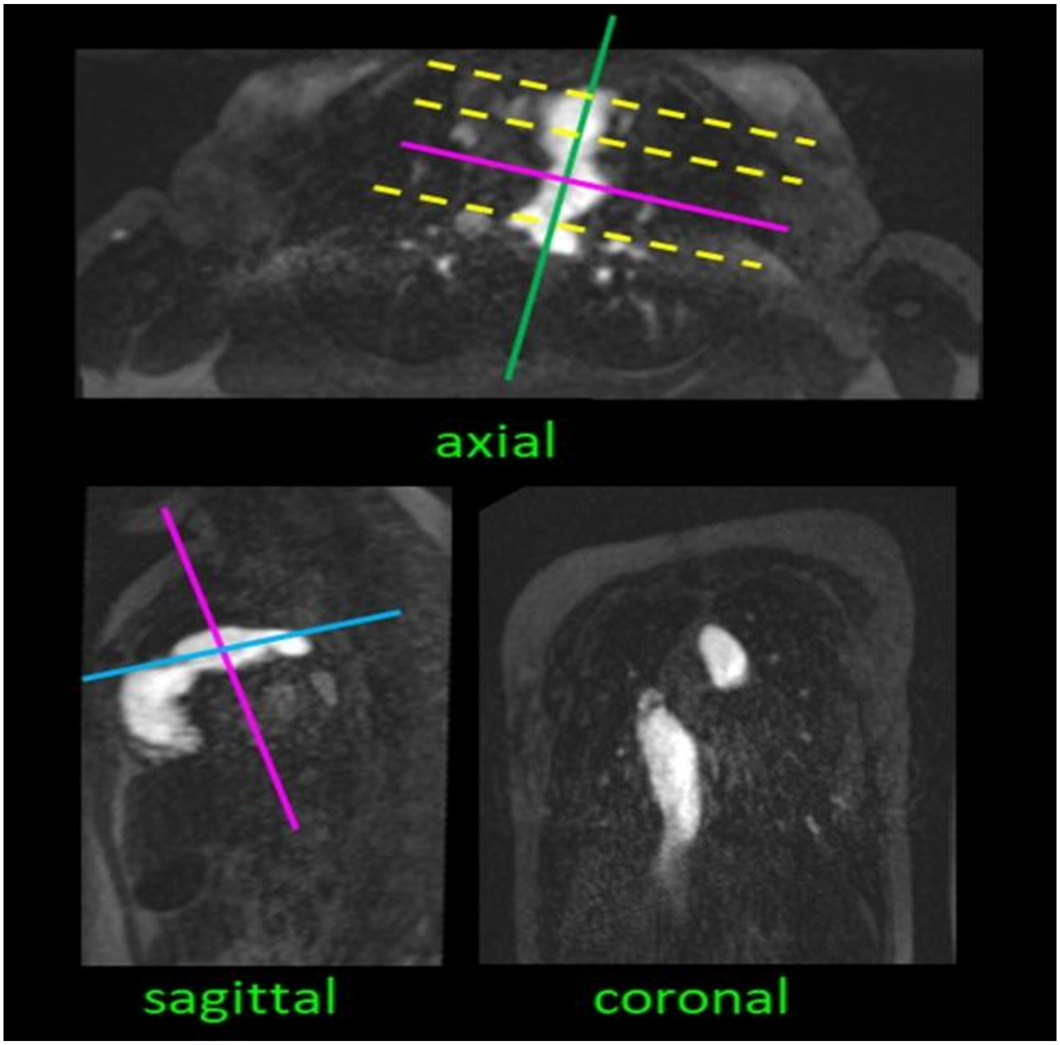

Figure 2. 2: Multiplanar reconstructed image of contrast-enhanced magnetic resonance angiography showing measurements at four points of RVOT for the defining of RVOT morphology.

According to measurements of RVOT at four points, we defined the morphological type of the RVOT within five shapes as a trapezoid-shaped (Type 1), tubular-shaped (type 2), inverted trapezoid (Type 3), apple shape (Type 4), hourglass shape (Type 5). To define the RVOT shape, more than a 50 % discrepancy in diameter is accepted as narrowing or dilatation. The RVOT shape is defined according to the measurements of RVOT at four points, as presented in **Figure 2.3.**

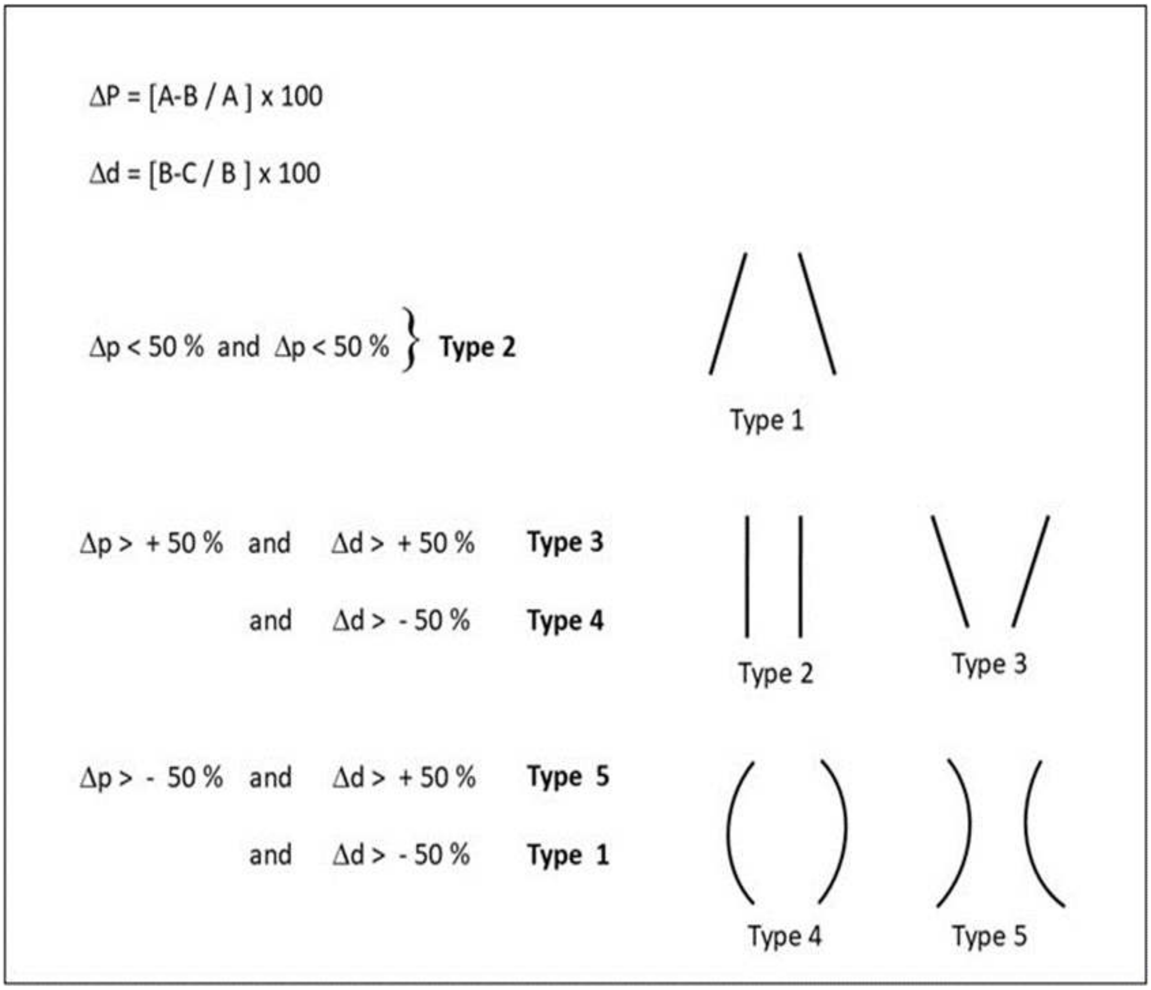

Figure 2. 3: The formulas and calculations (left column) and hand-drawn types of right ventricular outflow tract (right column).

Time resolve contrast-enhanced MRA at the pulmonary phase is selected to enhance the RVOT, and then a 3D reconstructed image is evaluated to define the type of RVOT. A 3D reconstructed image in STL format is used to produce a 3D printed model of RVOT. The flow chart of the clinical-radiological assessment of RVOT shape is presented in **Figure 2.4.**

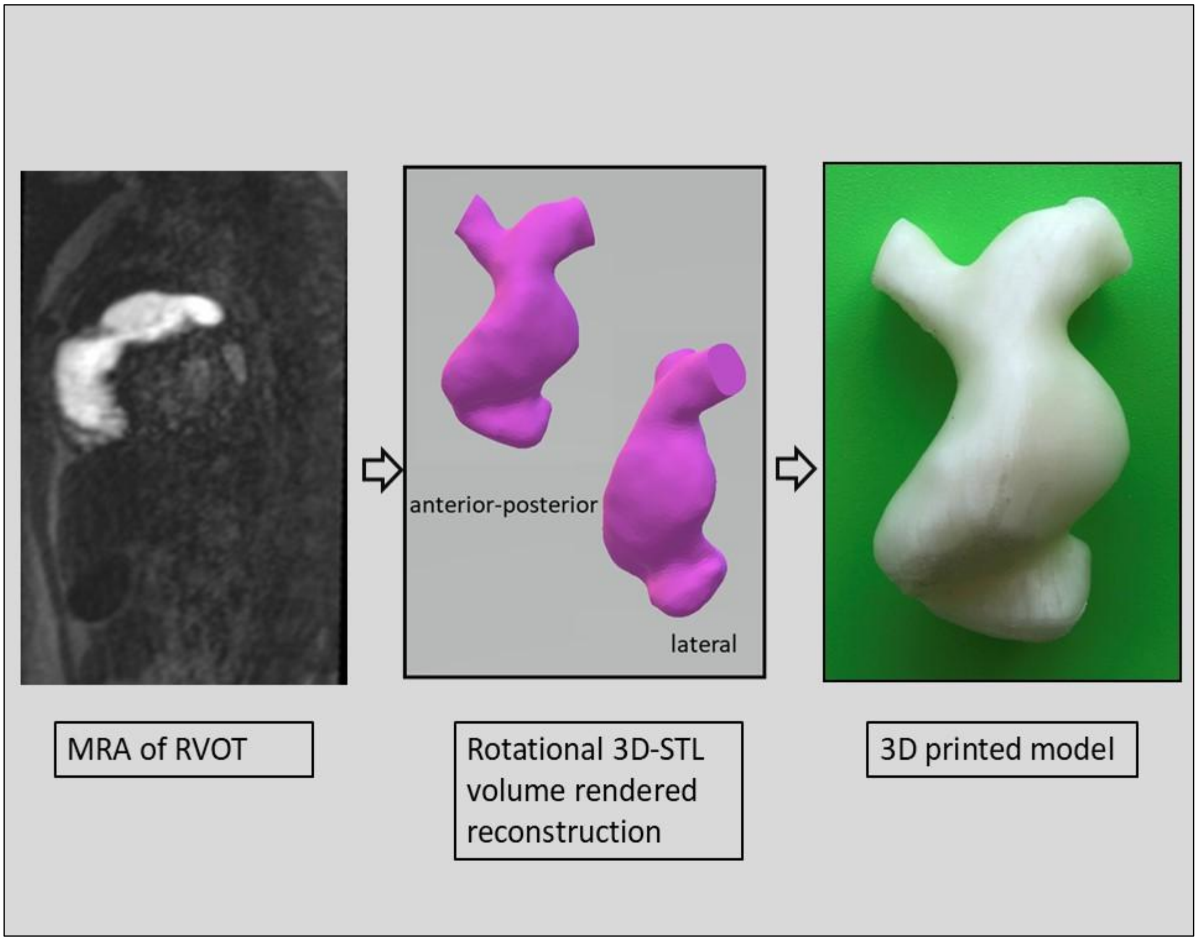

Figure 2. 4: The flow chart of the post-processing analyses to define the RVOT. Contrast-enhanced magnetic resonance angiography of the RVOT (left), 3D-segmented STL image of the RVOT (middle), and 3D printed model of RVOT.

2.2.4 3D Segmentation and Printing

The shape of the RVOT was also assessed and confirmed on rotational 3D volume-rendered images and 3D printed models. The most appropriate MRA phase dataset, which visualizes the region of interest, was selected for the 3D reconstruction. The open-source image processing software 3D Slicer 4.11 (http://www.slicer.org) was used for segmentation. A threshold range was created by selecting the pixel value of the blood pool region. Reconstruction was performed by following the continuity with this threshold in all slices of the dataset. The surface of the obtained raw virtual models was converted into a format that can be defined by unit triangles (STL). They were trimmed for rapid prototyping with open-sourced computer-aided design software (Free CAD; Munich, Germany). Physical 1:1 scale 3D models were obtained using the additive manufacturing methods technique. The fusion deposition modeling method was preferred, and Ultimaker S5 (Ultimaker B.V.; Geldermalsen, Netherlands) 3D printer with 0.4 nozzle size and 20 % grid infill was used. Physical 3D models were obtained by using a thermoplastic polyester (pure PLA) with 0.1 layer height and custom support **(Figure 2.5).**

Figure 2. 5: Five types of 3D printed RVOT morphology are shown. Trapezoid-shaped (Type 1), tubular-shaped (type 2), inverted trapezoid (Type 3), apple-shaped (Type 4), and hourglass-shaped (Type 5).

2.2.5 Evaluation of myocardial distortion

The feature tracking technique uses standard cine MRI images to track the motion of specific myocardial features over time, allowing the strain to be calculated to assess the deformation of the heart muscle (myocardium) during the cardiac cycle. In the context of cardiac imaging, "strain" refers to the percentage change in the length of a myocardial segment compared to its original length during the cardiac cycle. Strain is a measure of deformation and can be positive (stretching) or negative (contraction). The rate at which this deformation occurs is typically expressed per unit of time (e.g., per second). Strain evaluation provides detailed information about the mechanical function of the heart measured in different directions longitudinal, radial, and circumferential directions **(Figure 2.6).**

Two and four-chamber views were used for global longitudinal ventricular strain analyses, while four-chamber and short-axis views were used for global radial and circumferential ventricular strain analyses (**Figures 2.7 and 2.8**). Endocardial and epicardial borders were contoured manually during end-diastole and end-systole for analysis. The strain analyses were performed using the cardiac imaging software Circle (Circle Cardiovascular Imaging, Calgary, Alberta, Canada).

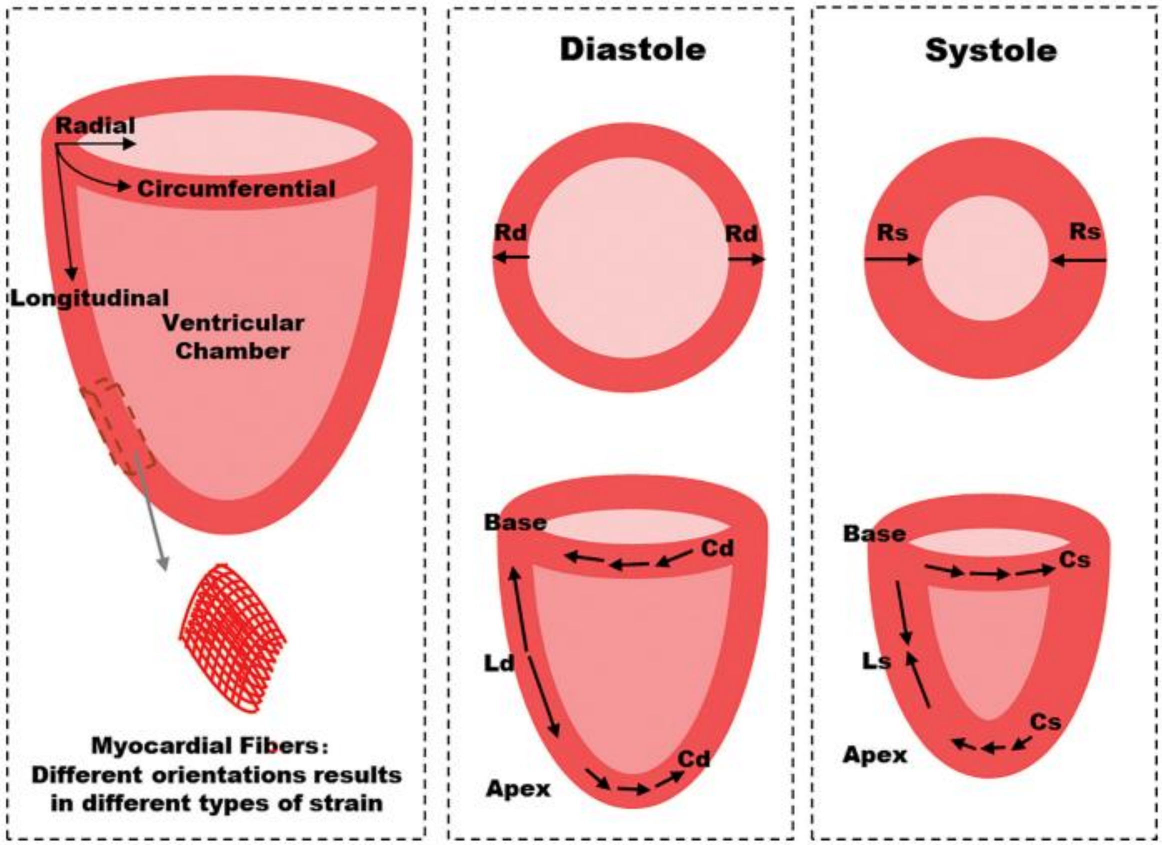

Figure 2. 6: The schematic myocardial strain diagram illustrates three main strain measurement types: longitudinal, circumferential, and radial. Longitudinal strain is measured from long-axis sections and describes the shortening or lengthening of the myocardium from the apex to the base of the heart. Circumferential and radial strains are assessed from short-axis sections, with circumferential strain representing deformation around the epicardial wall, while radial strain measures deformation towards the center of the ventricular cavity. This comprehensive approach to strain measurement provides valuable insights into the myocardial mechanics and function, as detailed in a study by Zhang X et al. (Zhang X et al. 2022).

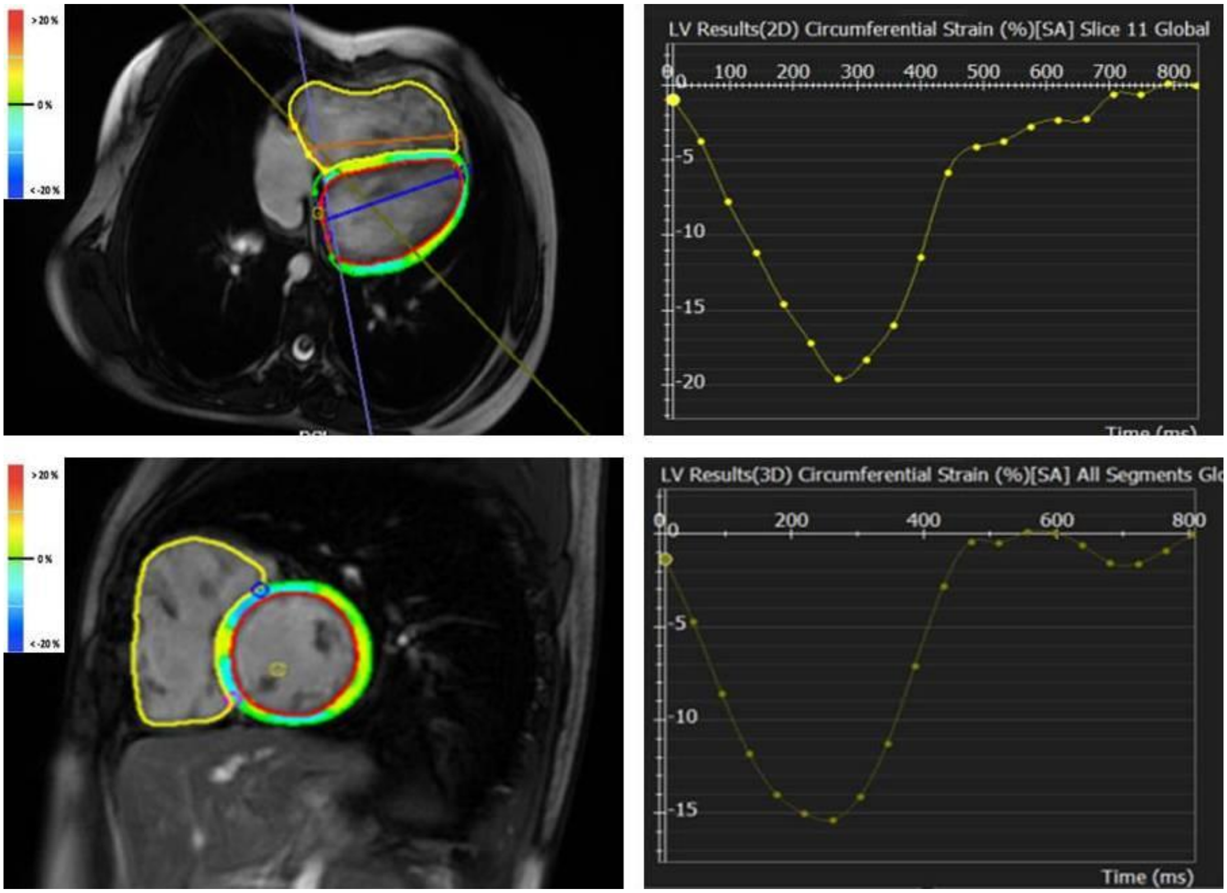

Figure 2. 7: Magnetic resonance imaging colored strain analysis of the left ventricle. A four-chamber cine steady-state free precession sequence (upper-left) provides the radial strain curve (upper-right), and a short-axis cine steady-state free precession sequence (lower-left) provides the circumferential strain curve (lower-right). The green line represents the outline of the left ventricular epicardium, while the red line represents the outline of the left ventricular endocardium. The yellow lines in the graphs (left-upper, left-lower) correspond to strain measurements from each ventricle.

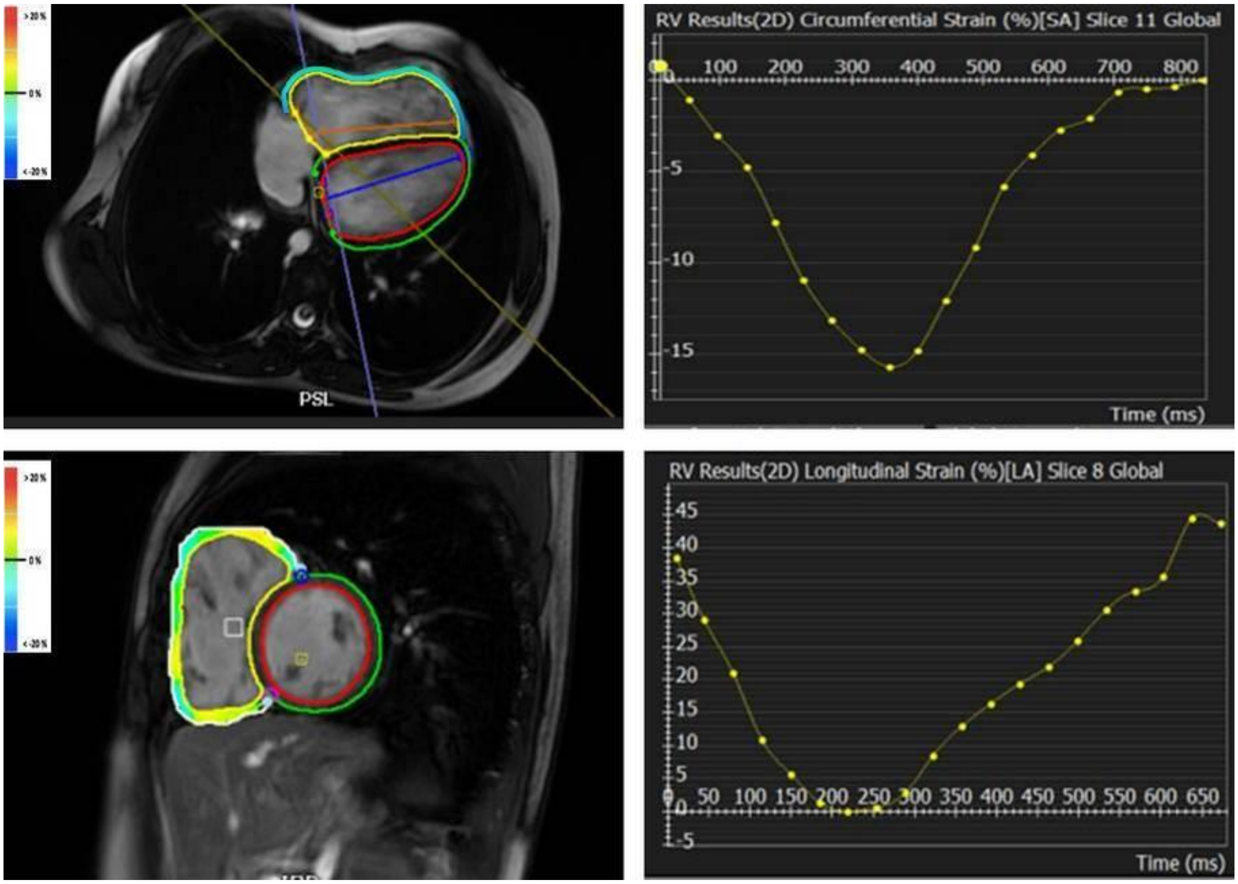

Figure 2. 8: Magnetic resonance imaging colored strain analysis of the left ventricle. A four-chamber cine steady-state free precession sequence (upper-left) provides the radial strain curve (upper-right), and a short-axis cine steady-state free precession sequence (lower-left) provides the circumferential strain curve (lower-right). The green line represents the outline of the right ventricular epicardium, while the red line represents the outline of the right ventricular endocardium. The yellow lines in the graphs (left-upper, left-lower) correspond to strain measurements of the right ventricle.

2.3 Results

The quantitative variables were presented as mean ± standard deviation or median (25th–75th percentiles). The Shapiro–Wilk normality test was applied to evaluate the data distribution. Spearman correlation analysis was performed to evaluate correlations. We compared cardiac MRI parameters and vessel measurements for five right ventricular outflow tract shapes. Kruskal–Wallis test was used to determine the heterogeneity of cardiac MRI parameters and vessel measurements. P< 0.05 indicates statistical significance. Data were analyzed using SPSS version 20.0 software (IBM Corporation, Armonk, NY).

2.3.1 Baseline characteristics of the patients

In total, 36 patients (M/F = 23/13) with repaired TOF for whom PVR was planned were included in this study. The mean age of patients was 17.6 ± 7.8 years (10–44 years), and the mean body surface area was 1.6 ± 0.3 m^2 (1.1–2.2 m^2). The mean age at initial surgical correction was 2.6 ± 2.1 years (1–9 years). The mean age of the patients during PVR was 18.1 ± 7.8 years (9–49 years). Transcatheter PVR was performed in 28 patients (M/F = 18/10), and surgical PVR was performed in 8 patients (M/F = 4/4). The mean age of the patients was 17.07 ± 7.5 years (10–44 years) vs. 19.63 ± 9.11 years (13–41 years) (*P* = 0.674) in transcatheter and surgical groups, respectively. The mean body surface area of the patients was 1.5 ± 0.3 m2 (1.1–2.0 m2) vs. 2.2 ± 1.7 m2 (1.3–2.3 m2) (*P* = 0.433) in the transcatheter and surgical groups, respectively. The mean age at initial surgical correction was 2.5 ± 1.8 years (1–8 years) vs. 3.2 ± 3.3 years (1–9 years) (*P* = 0.667), and the mean age at PVR was 17.7 ± 7.9 years (9–49 years) vs. 20 ± 7.6 years (12–32 years) (*P* = 0.571) in transcatheter and surgical groups, respectively. Age, body surface area, and ages at initial surgical correction and PVR were similar in the transcatheter and surgical groups.

In transcatheter PVR group, an Edwards Sapien® (Edwards Lifesciences, CA) pulmonary valve was used in 24 patients (29 mm in 17 patients and 26 mm in 7 patients), a Pulsta® (Tae Woong Medical Co, Gyeonggi-do, South Korea) pulmonary valve in 3 patients (32 mm in 2 patients, 30 mm in 1 patient), a Melody® (Medtronic Inc., Minneapolis, MN) pulmonary valve (24 mm) was used in 1 patient in the transcatheter group. In the surgical PVR group, Sorin bioSolo Smart valve was used in 2 patients (23 mm in 1 patient and 30 mm in 1 patient), a Bio mitral valve was used in 5 patients (27 mm in 1 patient, 29 mm in 3 patients and 31 mm in 1 patient) and a Carbo medics valve (29 mm) was used in 1 patient in the surgical group. An additional procedure was performed in 12 patients in the transcatheter group (ventricular septal defect closure in 2 patients, left pulmonary artery stenting in 8 patients, and balloon dilatation in 2 patients).

In the surgical PVR group, an additional surgical procedure was performed in 5 patients (ventricular septal defect closure in 2 patients, correction of partial anomalous pulmonary venous connection in 1 patient, aortic valve replacement in 1 patient, and subaortic wedge resection in 1 patient) (Figure 2.1).

2.3.2 Cardiac MRI characteristics

The cardiac volume, function, flow, and morphological characteristics of the native right ventricular outflow tract and branch pulmonary arteries were compared between transcatheter PVR and surgical PVR groups. The surgical PVR group was found to have lower circumferential and radial MRI strain for the right ventricle ($P = 0.045$ and $P = 0.046$, respectively). The biventricular end-diastolic volume index, end-systolic volume index, ejection fraction, and circumferential and radial MRI strain for the left ventricle were not significantly different. There was also no significant difference in pulmonary regurgitation between the two groups. However, the diameter and z-score of the left pulmonary artery were significantly lower in the transcatheter pulmonary group compared to the surgical group ($P = 0.021$ and $P = 0.048$, respectively). Concordantly, right pulmonary-to-left pulmonary artery flow and diameter ratio were significantly higher in the transcatheter group ($P = 0.044$ and $P = 0.002$, respectively). The diameter and z-score of the subvalvular right ventricular outflow tract and pulmonary valve annulus were higher in the surgical group compared to the transcatheter group ($P = 0.0001$ and $P = 0.003$ for diameter and $P = 0.0001$ and $P = 0.004$ for z-score, respectively). Cardiac MRI findings and measurements of the right ventricular outflow tract and branch pulmonary arteries are presented in **Table 2.2** and **Table 2.3.**

Table 2. 2: Cardiac magnetic resonance imaging findings in patients with repaired tetralogy of Fallot patients referred pulmonary valve replacement.

Parameters	**All patients (n=36)**	**Transcatheter PVR (n=28)**	**Surgical PVR (n=8)**	***P***
QRS duration, ms	139.22±22.01	139.42±20.61	140.24±31.02	0.984
RV EDVI, mL/m²	184.24±41.73	179.61±31.11	200.41±67.82	0.425
RV ESVI, mL/m²	111.10±29.72	106.84±21.55	126.32±47.96	0.296
RV EF, %	40.30±6.64	41.11±5.71	37.87±9.12	0.355
LV EDVI, mL/m²	92.40±16.82	92.14±15.40	93.56±22.32	0.875
LV ESVI, mL/m²	48.97±11.21	48.21±9.31	51.62±16.84	0.456
LV EF, %	47.22±6.25	47.71±5.23	45.42±90	0.502
RV strain- global circumferential (%)	-14.65±3.08	-15.20±2.81	-12.61±3.42	0.045
RV strain- global radial (%)	24.212±6.037	25.250±5.686	20.36±6.13	0.046
LV strain-global circumferential (%)	-14.13±3.47	-13.81±3.39	-15.24±3.78	0.499
LV strain-global radial (%)	25.41±8.41	24.56±817	28.57±9.16	0.549
PR fraction, %	48.62±9.63	46.91±8.94	54.36±10.30	0.099

Table 2. 3: Measurements of the right ventricular outflow tract and branch pulmonary arteries in patients with repaired tetralogy of Fallot patients referred pulmonary valve replacement.

Parameters	**All patients (n=36)**	**Transcatheter PVR (n=28)**	**Surgical PVR (n=8)**	***P***
RPA/LPA blood flow ratio	2.38±1.21	2.51±1.29	1.73±0.56	0.044
RPA/LPA diameter ratio	1.21±0.40	1.32±0.41	0.93±0.24	0.002
RPA diameter (mm) (narrowest point)	19.23±4.44	19.21±4.46	19.20±51	0.982
RPA diameter,z-score	2.0±1.59	2.1±1.63	1.67±1.48	0.498
LPA diameter (mm) (narrowest point)	17.6±5.2	16.7±5.2	20.9±3.7	0.021
LPA diameter, z-score	-1.27±8.61	0.98±1.76	3.15±2.52	0.048
Subvalvular RVOT (mm)	32.91±5.82	31.31±5.24	38.91±3.33	0.0001
Subvalvular RVOT (z-score)	2.86±1.51	2.53±1.54	4.01±0.47	0.0001
Pulmonary valve annulus (mm)	28.81±5.32	27.44±4.62	33.86±4.30	0.003
Pulmonary valve annulus (z-score)	1.51±1.75	1.17±1.8	2.66±0.89	0.004
Supravalvular MPA (mm)	20.16±5.50	26.80±4.83	32.15±6.32	0.054
Supravalvular MPA (z-score)	1.41±1.67	1.16±1.59	2.27±1.75	0.137
Distal MPA (mm)	28.16±6.44	27.22±5.50	31.30±8.64	0.242
Distal MPA (z-score)	1.31±1.90	1.26±1.70	1.82±2.56	0.570

2.3.3 RVOT Morphology and correlation with cardiac MRI characteristic

The most common type of right ventricular outflow tract shape was trapezoid-shaped type 1 (n=14, 38.9%), followed by tubular-shaped type 2 (n=8, 22.2%), hourglass-shaped type 5 (n=7, 19.4%), inverted trapezoid-shaped type 3 (n=6, 16.7%) and apple-shaped type 4 (n=1, 2.8%). In the transcatheter group, the most common type of right ventricular outflow tract shape was trapezoid-shaped type 1 (n=10, 35.7%), followed by tubular-shaped type 2 (n=7, 25%), inverted trapezoid-shaped type 3 (n=6, 21.4%) and hourglass-shaped type 5 (n=5, 17.9%). In the surgical group, the most common type of right ventricular outflow tract shape was trapezoid-shaped type 1 (n=4, 50 %), followed by hourglass-shaped type 5 (n=2, 25%), tubular-shaped type 2 (n=1, 12.5%) and apple-shaped type 4 (n=1, 12.5%). End-diastolic volume index, circumferential, and global MRI strain for the right ventricle and left pulmonary artery diameter were significantly different between the right ventricular outflow tract types (P=0.046, P=0.046, P=0.049 and P = 0.046, respectively). Among all right ventricular outflow tract types, the tubular-shaped type 2 right ventricular outflow tract had the smallest right ventricle end-diastolic volume index (157, 88 ± 24.08 mL/m^2), while the hourglass-shaped type 5 right ventricular outflow tract had the largest right ventricle end-diastolic volume index (201.29 ± 49.95 mL/m^2). The lowest right ventricle circumferential strain was in the inverted pyramid-shaped type-3 right ventricular outflow tract, and the highest strain was observed in hourglass-shaped type 5. The highest right ventricle radial strain was observed in the inverted pyramid-shaped type 3 right ventricular outflow tract, and the lowest value was observed in hourglass- shaped type 5. The lowest left pulmonary artery diameter was observed in the tubular-shaped type 2 right ventricular outflow tract, and the highest was the inverted pyramid-shaped type 3. A comparison of right ventricular outflow tract types in terms of cardiac MRI parameters, measurements of the right ventricular outflow tract, and branch pulmonary arteries are presented in **Table 2.4.**

Table 2. 4: Comparison of different types of right ventricular outflow tract morphology in patients with repaired tetralogy of Fallot who referred pulmonary valve replacement

Parameter	Type 1 (n=14, 38.9 %)	Type 2 (n=8, 22.2 %)	Type 3 (n=6, 16.7 %)	Type 4 (n=1, 2.8 %)	Type 5 (n=7, 19.4 %)	*P*
RV EDVI, mL/m²	180.79±39.98	157.88±24.08	192.83±32.37	172	201.29±49.95	0.046
RV ESVI, mL/m²	108.93±29.08	93.88±20.53	115.00±24.22	170	123.43±34.16	0.082
RV EF, %	41.00±7.61	41.00±7.05	40.50±5.99	37	38.57±5.740	0.923
LV EDVI, mL/m²	87.64±15.77	87.88±13.31	99.83±21.73	106	99.01±17.22	0.343
LV ESVI, mL/m²	46.5±11.13	46.75±8.53	48.83±9.73	56	55.57±14.87	0.450
LV EF, %	47.21±6.99	47.02±2.26	50.5±6.59	48	44.43±7.41	0.557
LV strain-global circumferential, %	-13.96±3.16	-14.87±3.43	-15.42±0.98	-15.34	-12.58±4.98	0.499
LV strain-global radial, %	25.33±7.28	27.93±9.84	26.76±1.27	25.54	21.7±11.43	0.549
RV strain-global circumferential, %	-14.39±3.28	-16.26±1.36	-16.18±2.59	-15.42	-12.25±3.23	0.046
RV strain-global radial, %	23.76v6.49	26.57±2.89	27.98±5.45	26.32	19.65±6.04	0.049
PR fraction, %	49.93±8.41	44.5±8.6	50.52±11.07	59	47.29±11.96	0.534
RPA/LPA blood flow ratio	1.29±0.36	1.37±0.37	0.99±0.36	1.09	1.25±0.31	0.354
RPA diameter, mm (narrowest point)	18.79±4.27	17.62±2.98	20.67±6.38	17.5	20.93±4.63	0.583
RPA diameter, z-score	1.82±1.11	1.59±1.12	2.6±2.99	0.57	2.53±1.35	0.554
LPA diameter, mm (narrowest point)	16.32±4.53	14.94±3.28	22.67±6.43	19	15.57±4 .31	0.046
LPA diameter, z-score	1.37±2.56	0.41±1.11	3.19±2.05	1.24	1.38±1.62	0.197

2.4 Discussion

In this study, we aimed to investigate the differences in preprocedural MRI characteristics (volume, function, strain) and morphology of the right ventricular outflow tract and branch pulmonary arteries in patients in whom surgical or transcatheter PVR was evaluated.

2.4.1 Cardiac magnetic resonance imaging strain analysis

Myocardial strain analysis was first applied to echocardiography to represent the deformation of cardiac fibers through the cardiac cycle (Dandel M et al. 2009). Cardiac MRI strain analysis allows reproducible and quantitative assessment of cardiac deformation without the need for additional time or sequences (Maceira AM et al. 2018). Strain measurement is suggested to be more sensitive than ejection fraction for the detection of functional cardiac abnormalities. Strain measurement can be used as an early indicator of ventricular dysfunction before overt changes in ejection fraction (Toro-Salazar et al. 2013; Negishi K et al. 2013; Thavendiranathan P et al. 2014). A limited number of studies evaluate myocardial strain in patients with repaired TOF (Orwat et al. 2016; Anwar S et al. 2017). The impaired biventricular strain has been reported to be associated with adverse outcomes, including sudden cardiac death in older patients with repaired TOF (Orwat et al. 2016). Moceri et al. (Moceri P et al. 2021) compared chronic volume loading in an atrial septal defect with a repaired TOF in terms of the right ventricular deformation. In patients with repaired TOF, longitudinal and circumferential strains were found to be markedly reduced. However, patients with atrial septal defects and controls had similar circumferential and longitudinal strains. To the best of our knowledge, no MRI study has compared the strain characteristics of patients undergoing transcatheter or surgical pulmonary valve replacements. We found that the global circumferential and radial MRI strain values for the right ventricle decreased in patients selected for surgical pulmonary valve replacement. However, the biventricular end-diastolic volume index, end-systolic volume index, ejection fraction, and MRI strains (circumferential and radial) for the left ventricle were similar between the transcatheter and surgical groups. In a study by Zablah et al. (Zablah JE et al. 2017), the surgical PVR group had higher right ventricular volume than the transcatheter group at referral. However, the biventricular function was not significantly different. Right ventricular outflow tract fibrosis and aneurysm were reported to be associated with right ventricle dysfunction in repaired TOF patients with significant pulmonary regurgitation (Davlouros PA et al. 2002; Wald RM et al. 2009; Babu-Narayan SV et al. 2006; Gatzoulis MA et al. 2000; Valente AM et al. 2014). In our study, the poorer MRI strain findings in the surgical group compared to the transcatheter group might be related to a dilated right ventricular outflow tract and right ventricular remodeling.

2.4.2 Right ventricular outflow tract morphology

The shape of the native right ventricular outflow tract and the branch pulmonary arteries were also assessed in this study. The right ventricular outflow tract was larger in the valvular and subvalvular areas. Furthermore, we found that right ventricular outflow tract types had significantly different end-diastolic volume index, right ventricular circumferential and global MRI strain, and left pulmonary artery diameter. The shape of the right ventricular outflow tract, which was classified into five groups by Schievano et al. (Schievano S et al. 2007), has been suggested to affect surgical planning and the success of pulmonary valve replacement. A pyramid-shaped type 1 right ventricular outflow tract was found to be associated with a severe pulmonary regurgitation fraction. The tubular-shaped type 2 right ventricular outflow tract is felt to be the most suitable type of right ventricular outflow tract for stent placement. However, the right ventricular outflow tract type was heterogeneous; some patients had a native right ventricular outflow tract while others had a conduit (Schievano S et al. 2007). In another study, the pyramid-shaped type 1 right ventricular outflow tract was considered unsuitable for the transcatheter approach because of the risk of stent dislocation (Chung R, Taylor AM. 2014). Van De Bruaene et al. (Van De Bruaene A et al. 2019) showed that convergent anatomy or a pyramid-shaped type 1 right ventricular outflow tract was associated with a higher pulmonary regurgitation fraction. In another study by Shen et al. (Shen WC et al. 2020), right ventricular outflow tract diameter and shape correlated with right ventricle volume in repaired TOF with a native right ventricular outflow tract.

2.4.3 Branch pulmonary artery stenosis and blood flow distribution

Residual branch pulmonary artery stenosis is a common pathology in repaired TOF (McElhinney DB et al. 1998). In this study, we found that the diameter of the left pulmonary artery was significantly lower in patients selected for the transcatheter approach. In parallel to this result, the right-to-left pulmonary artery diameter and flow ratio were significantly higher in the transcatheter group. Flow discrepancy and ventilation/perfusion mismatch between the lungs are suggested to be associated with the severity of pulmonary regurgitation, arrhythmia, and the need for early PVR (Valente AM et al. 2014; Harris MA et al. 2011; Hickey EJ et al. 2009; Hennein HA et al. 1995). In a study by Sutton et al., blood flow discrepancy and exercise capacity were shown to be improved after the dilatation of the branch pulmonary artery stenosis by balloon angioplasty (Sutton NJ et al. 2008). Severe branch pulmonary artery stenosis with a diminished pulmonary flow of less than 30% toward the affected lung was suggested as a criterion for PVR (Geva T 2013). Furthermore, pulmonary artery balloon "dilatation or stent implementation is recommended in patients with a relative flow discrepancy between the two lungs of 65/35% (~ 1.857) or worse (Ferrari I et al. 2020). In our study, all patients who needed branch pulmonary artery stenting or balloon dilatation were in the transcatheter approach group. Some authors suggest a surgical approach as the preferred modality in patients with pulmonary artery branch stenosis (Ou-Yang WB et al. 2020). However, the transcatheter approach may be preferred because it has the advantage of allowing pulmonary artery stenting or balloon dilatation in patients with pulmonary stenosis in the same session as pulmonary valve replacement.

Our study has several limitations, including a small number of patients, a lack of post-procedural cardiac MRI follow-up, and the absence of internal validation with a second reader. Another possible limitation is that measurement of the right ventricular outflow tract and branch pulmonary arteries is acquired randomly in any phase of the cardiac cycle in MRA. The observational nature of the study may have led to bias in patient selection for the transcatheter and surgical groups, which is a further limitation.

In conclusion, preprocedural MRI strain, right-to-left pulmonary artery flow ratio and morphological features of the right ventricular outflow tract and branch pulmonary arteries were different in patients planned to have surgical or transcatheter pulmonary valve replacement. This suggests that MRI strain analysis may be a useful tool for quickly and accurately evaluating early right ventricular dysfunction. Furthermore, this study provides evidence for the use of the transcatheter approach as an effective treatment option for patients, as it can minimize the risk of complications. Our study suggests that the transcatheter approach may be recommended in patients with branch pulmonary artery stenosis due to its ability to provide both PVR and branch pulmonary artery stenting/balloon dilatation in the same session. This approach reduces the length of the overall procedure, minimizes the risk of complications, and may improve treatment outcomes.

Cardiac MRI is the gold standard imaging technique for quantitatively assessing ventricular volume, function, and pulmonary regurgitation fraction. It has become a preferred noninvasive imaging tool for morphologic and physiologic evaluation of repaired TOF. It allows quantification of blood flow distribution of the branch pulmonary artery, which is essential for evaluating residual branch pulmonary stenosis. This is also important for decisions on subsequent interventions (Geva T, 2013). Magnetic resonance angiography with multiplanar reconstruction and 3-D volume-rendered images is a decision-making application that can assess the suitability for transcatheter PVR (Chung R, Taylor AM. 2014). It is also helpful for determining the morphology of the right ventricular outflow tract or branch pulmonary arteries (Ferrari I et al. 2020).

Chapter 3

3 EVALUATION OF ATRIAL AND VENTRICULAR MYOCARDIAL DISTORSION AFTER PVR IN PATIENTS WITH REPAIRED TETRALOGY OF FALLOT BY FEATURE TRACKING STRAIN TECHNIQUE

3.1 Introduction

Pulmonary valve replacement (PVR) is recommended for patients with repaired tetralogy of Fallot (TOF). Surgical correction often results in pulmonary regurgitation, leading to ventricular dilatation, systolic dysfunction, atrial enlargement, and adverse clinical outcomes such as right heart failure, arrhythmias, and sudden cardiac death (Mongeon FP et al.2019; Stout KK et al. 2019; Baumgartner H et al. 2021). However, the impact of PVR on long-term adverse clinical outcomes and reverse atrial and ventricular remodeling is still scarce and controversial (Ferraz Cavalcanti PE et al.2013; Van den Eynde J et al. 2022). Demonstrating early systolic and diastolic dysfunction by myocardial strain assessment that defines the deformation of fibers through the cardiac cycle before the impairment of ejection fraction is crucial for comprehensive management and risk stratification (Scatteia A, Baritussio A, and Bucciarelli-Ducci C. 2017). However, the complex geometric structure of the right ventricle and limited acoustic window limit the evaluation of myocardial distortion with conventional echocardiography techniques. Cardiac magnetic resonance imaging (MRI) is widely accepted as the gold standard imaging technique assessing biventricular volume and function, blood flow, and pulmonary regurgitation. It plays a crucial role in clinical decision-making regarding the timing of PVR, whether surgical or transcatheter, in line with current guidelines (Stout KK et al. 2019; Baumgartner H et al. 2021). The main advantage of the technique over transthoracic echocardiography is that it provides increased spatial resolution for the myocardial wall of both ventricles and atria. Recent advancements in non-invasive imaging techniques have also facilitated the direct assessment of atrial and ventricular deformation by feature-tracking strain through cardiac MRI (Balasubramanian S et al. 2018; Hu L et al. 2021; Orwat et al. 2016). The atrial strain offers insights into atrial function across various phases of the cardiac cycle (Kessler Iglesias C et al. 2023) (**Figure 3.1**). Reservoir function in systole reflects atrial compliance; passive conduit function in early diastole indicates ventricular relaxation and chamber stiffness; and booster function represents intrinsic atrial contractility and ventricular compliance through atrial contraction in late diastole (Hu L et al. 2021; Orwat et al. 2016; Hasselberg NE et al. 2021; Thomas L et al. 2019). It has been of significant importance in assessing atrial remodeling response to PVR in patients with repaired TOF in recent years. To the best of our knowledge, only one previous study has evaluated the atrial strain changes by cardiac MRI after PVR (Latus H et al. 2021). In addition to atrial strain, the evaluation of ventricular strain is considered a more sensitive indicator of ventricular function than volumetric parameters (Balasubramanian S et al. 2018). Although the left and right ventricular strain was significantly associated with adverse outcomes (Monti CB et al., 2020; Zhuang B et al. 2020), the improvement in global right ventricle strain following PVR in patients with repaired TOF remains poorly defined (Van den Eynde J et al. 2022).

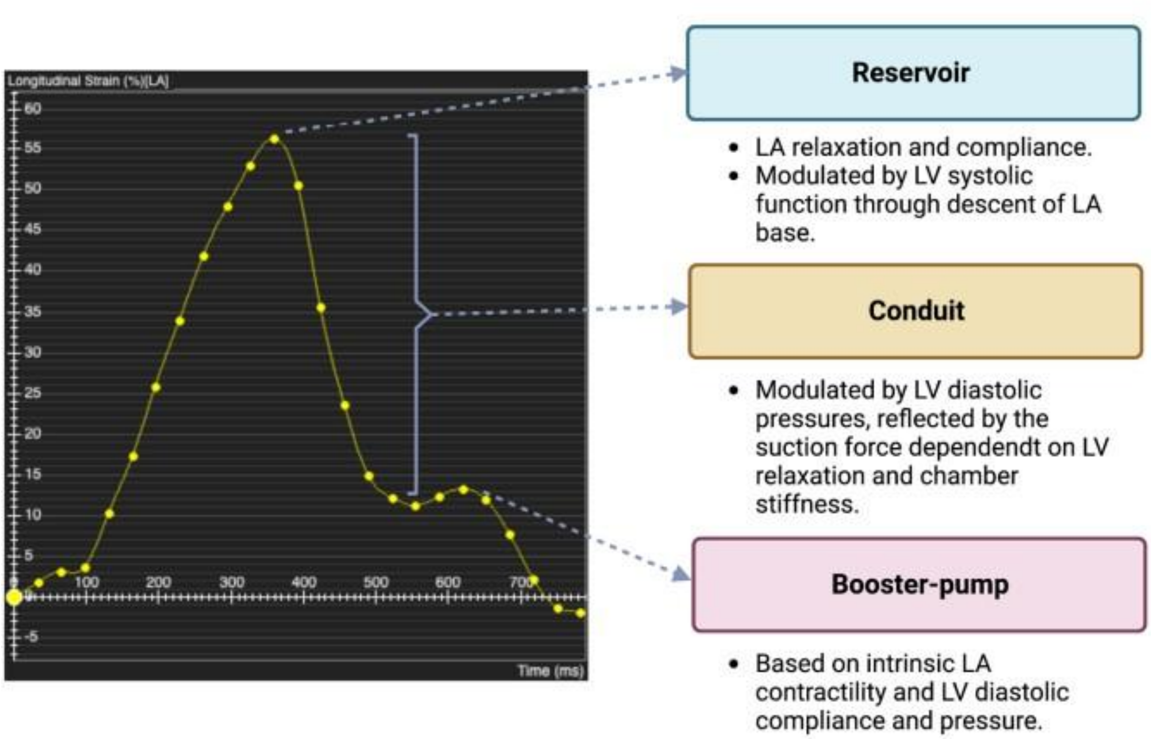

Figure 3.1: Atrial strain line graph depicting global longitudinal left atrial strain across cardiac cycle (yellow dots). Reservoir strain is defined as the peak value of the initial diastolic phase, booster-pump strain is the peak value of the subsequent systolic phase, and conduit strain is calculated as the difference between the reservoir strain and the booster-pump strain. This comprehensive approach to strain measurement provides valuable insights into the atrial mechanics and function as detailed in a study of Kessler Iglesias C et al. (Kessler Iglesias C et al. 2023

3.2 Materials and Methods

3.2.1 Patient groups and data collection

The patients who underwent cardiac MRI within one year before and after PVR were retrospectively reviewed. A total of 18 patients who underwent transcatheter PVR were included in the study. All patients had the same surgical history of ventricular septal defect closure and the right ventricular outflow tract patch augmentation. Patients with the right ventricle-to-pulmonary artery conduit and valve-in-valve implants were excluded.

Demographic data (gender, age) and clinical information (type of surgical procedures, echocardiography, electrocardiography, and cardiac catheterization findings) of the patients were collected from the hospital database system and recorded. The weight and height of the patients were recorded to calculate body surface area for indexed values.

The indications of transcatheter PVR were moderate-to-severe pulmonary regurgitation (regurgitation fraction by cardiac MRI ≥25%) and at least 2 of the following conditions: right ventricle end-diastolic volume index ≥150 ml/m2, right ventricle end-systolic volume index ≥80 ml/m2, right ventricle ejection fraction ≤47%, left ventricle end-diastolic volume index ≤65 ml/m2, severe branch pulmonary artery stenosis (preferential blood flow less than 30% to affected lung) and QRS duration longer than 160 ms on the electrocardiogram. The patients with pulmonary stenosis who had the indication for PVR were excluded. The cardiac MRI examination performed longer than one-year pre-procedure and post-procedure were excluded.

3.2.2 Cardiac magnetic resonance imaging technique

Biventricular volume, function, strain, and blood flow analyses were performed by using the cardiac imaging software Circle (Circle Cardiovascular Imaging, Calgary, Alberta, Canada). The evaluation of cardiac MRI data was performed using the same technique as mentioned in Chapter 2.2.2.

3.2.3 Cardiac magnetic resonance imaging evaluation

Cardiac MRI protocol evaluation and the parameters and the technique are performed according to the same protocol mentioned in Chapter 2.2.3 (**Table 2.1**).

Correction of the contouring performance was also performed manually to ensure the accuracy of cardiac MRI parameters (volume, function, and flow analyses). All volumetric data were indexed and recorded according to the body surface area (using the Mosteller formula). For the flow analysis, the contour of the main pulmonary artery was traced automatically. The pulmonary regurgitation fraction was calculated automatically. The formula is diastolic backward flow/systolic forward flow x 100 %.

3.2.4 Evaluation of myocardial distortion

Cine cardiac MRI data were used to evaluate strain analyses. Left and right ventricular strains were computed using the two-chamber, four-chamber, and short-axis cine images, while only the four-chamber cine image was used for left and right atrial strain. For atrial strain assessment, endocardial contours were traced using semi-automatic detection by locating the tricuspid and mitral valves manually. Endocardial and epicardial boundaries at end-diastole and end-systole were traced automatically. The propagated myocardial tissue through the cardiac cycle was controlled by the operator and border contours were corrected as required. Global atrial strain values were automatically derived by the software and controlled. Caval veins, coronary sinus, and pulmonary veins were excluded at their junction to the atrium (**Figure 3.2**). The atrial strain was evaluated in terms of strain parameters as a reservoir (the passive left atrial expansion with blood from the pulmonary veins during left ventricle contraction), conduit (the passive filling of blood from the left atrium to the left ventricle in early-mid left ventricle diastole), and pump strain (the atrial kick in the late, active left ventricle diastole) function. Reservoir and pump strain were determined from the highest and lowest peak on the atrial strain curve. Conduit strain was defined as the difference between the reservoir and pump strain. Reservoir, conduit, and pump strain rates were determined as the first positive systolic peak, earliest negative diastolic peak, and late negative diastolic peak, respectively.

Two and four-chamber cine views were used for global longitudinal ventricular strain analyses, while four-chamber and short-axis cine views were used for global radial and circumferential ventricular strain analyses. The phase with the largest blood pool area in the middle of the cavity was defined as the end-diastolic phase and the smallest as the end-systolic phase. The endocardium of the ventricles is contoured automatically by the threshold-based segmentation method. The trabeculae and papillary muscles were included in the blood pool. The reference regions at the superior and inferior insertion points of the septum were pointed and drawn manually. The contour of the myocardium for the entire cardiac cycle is propagated automatically. After the contouring was controlled, boundary editing was performed manually, if needed. The software automatically generated the biventricular global radial, circumferential, and longitudinal strain curves. The countering of left and right ventricles are shown in **Figure 3.3 and Figure 3.4.**

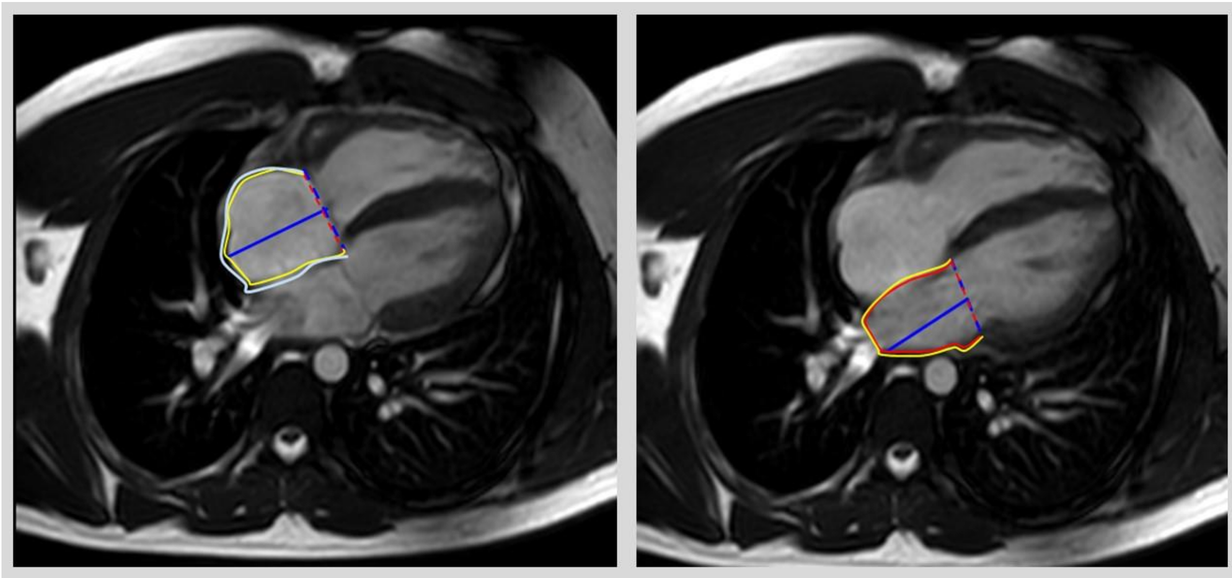

Figure 3.2: Representative feature-tracking strain cardiac MRI measurement technique for right (left) and left atria in four-chamber cine images

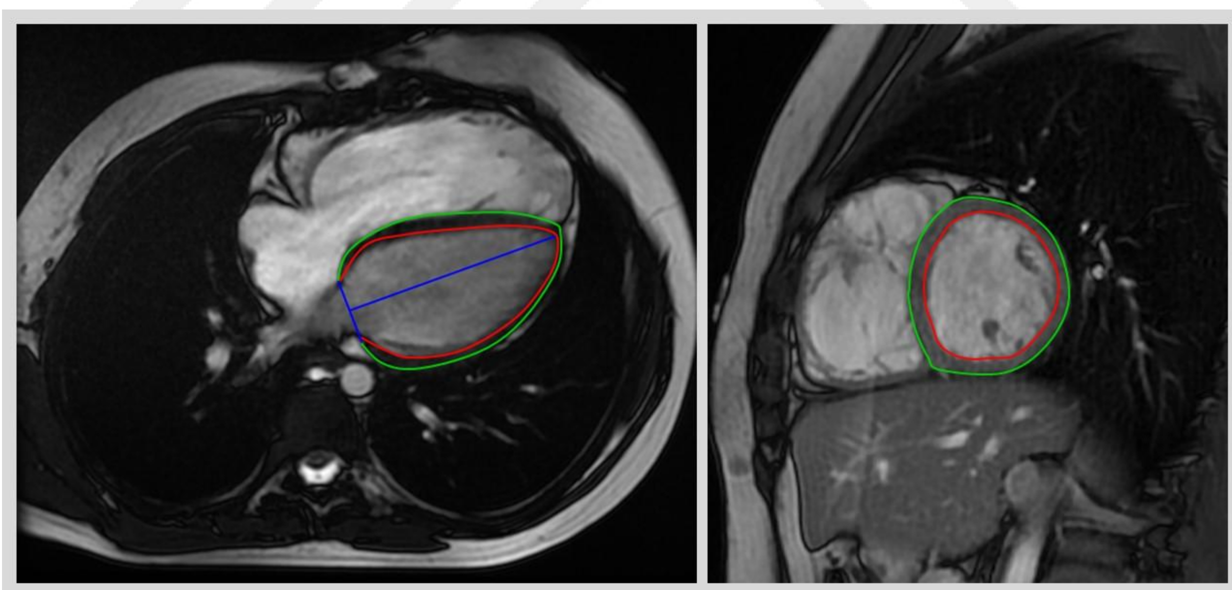

Figure 3.3: Strain measurement of the left ventricle in four-chamber (left) and short axis (right) cine steady-state free precession images to produce the circumferential longitudinal and radial strain curves. The red curve indicates the endocardial border, while the green curve indicates epicardial contours.

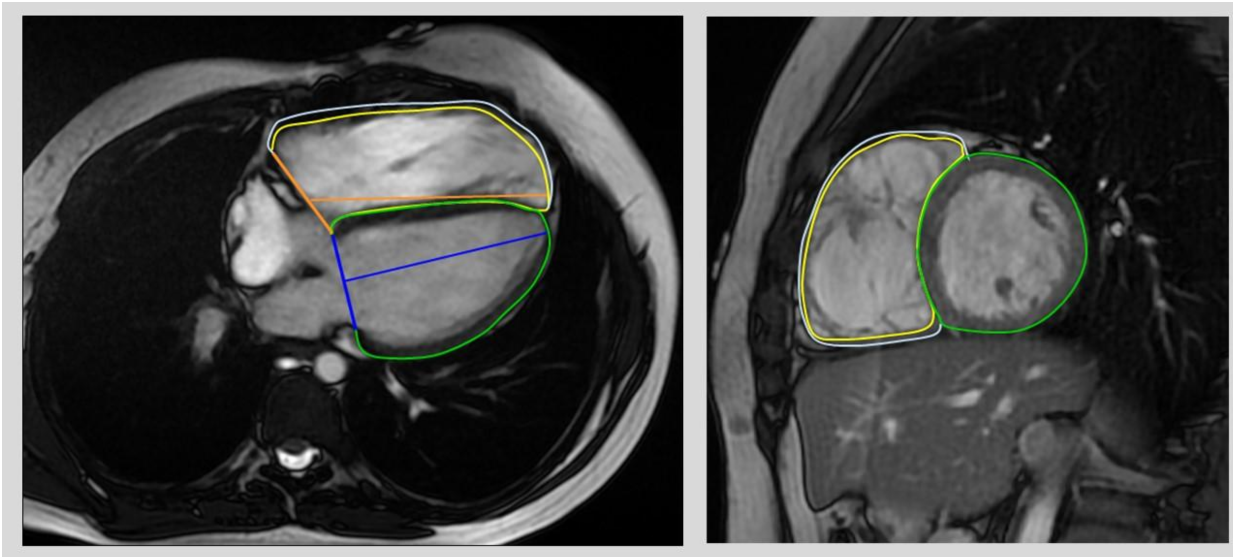

Figure 3.4: Strain measurement of the right ventricle in four-chamber (left) and short axis (right) cine steady-state free precession images to produce the circumferential longitudinal and radial strain curves. The yellow curve indicates an endocardial border, while the white curve indicates epicardial contours.

The analysis of the obtained data was assessed using SPSS version 20.0 software (IBM Corporation, Armonk, NY, USA). The Kolmogorov–Smirnov normality test was applied to evaluate the data distribution. Normally distributed continuous variables are presented as mean ± standard deviation or as median with interquartile range (IQR 25-75) in non-normally distributed data. The Wilcoxon rank-sum test was used to compare the strain and cardiac MRI parameters (volume, function, and pulmonary regurgitation fraction) before and after pulmonary valve replacement. Results with a P value <0.05 were considered statistically significant.

3.3 Results

In total, 18 patients (M/F=11/7) with repaired TOF for whom transcatheter PVR was performed were included in this study. Primary surgery was performed at a median of 18 months of age (interquartile range, 12–24 months). All patients had transannular patch augmentation with the closure of the ventricular septal defect. Transcatheter PVR was performed at a median of 14.5 months of age (interquartile range, 12–16 months). Edwards Sapien® (Edwards Lifesciences, CA, USA) pulmonary valve was used in 12 patients (29 mm in 10 patients and 26 mm in 2 patients), Myval™ T.H.V. (Meril Life Sciences Pvt Ltd, Vapi, Gujarat, India) pulmonary valve in 6 patients (32 mm in 2 patients, 29 mm in 4 patient). Seven patients had left pulmonary artery stenting during transcatheter PVR (one patient with Myval™ T.H.V. vs. six patients with Edwards Sapien® pulmonary valve). The duration between the first cardiac MRI examination and transcatheter PVR was 6.5 (interquartile range, 4.75–11.00) months vs. transcatheter PVR, and the second cardiac MRI examination was 11.50 (interquartile range, 9.25–12.00) months. The first cardiac MRI was performed at a median age of, and the mean body surface area was 1.49 (interquartile range, 1.12–1.62) m^2. The median age of the patients at first and second cardiac MRI was 13.5 (interquartile range, 10–15) vs. 15.00 (interquartile range, 12.75–16.00) years. Demographic data of the patients are presented in **Table 3.1.**

Table 3.1: Demographic data of the study group

Parameters	
N (male/female)	18 (11/7)
Age of surgery, months	18.00 (12.00–24.00)
Age of PVR, years	14.5 (12.00–16.00)
Age of first cardiac MRI, years	13.50 (10.00–15.00)
Body surface area at first cardiac MRI, m^2	1.49 (1.12–1.62)
Age of second cardiac MRI, years	15.00 (12.75–16.00)
Body surface area at second cardiac MRI, m^2	1.58 (1.41–1.75)
Duration between first cardiac MRI and PVR (months)	6.50 (4.75–11.00)
Duration between PVR and first cardiac MRI (months)	11.50 (9.25–12.00)

3.3.1 Ventricular Volume, Function, and Pulmonary Regurgitation Fraction

Right ventricle parameters, including right ventricle end-diastolic volume index, right ventricle end-systolic volume index, and right ventricle stroke volume index, showed significant improvement. **Table 3.2** demonstrates the cardiac MRI parameters before and after transcatheter pulmonary valve replacement. There was no significant difference in the right ventricular ejection fraction (41.50 vs. 43.50, P = 0.076). A significant decrease was observed only in left ventricle end-systolic volume index, while no difference was observed in left ventricle end-diastolic volume index, end-systolic volume index, left ventricle stroke volume index, left ventricle ejection fraction (88.00 vs. 82.00, P = 0.117; 46.00 vs. 41.00, P = 0.017; 42.00 vs. 39.50, P = 0.341; 49.50 vs. 51.00, P = 0.074). As expected, the pulmonary regurgitation fraction showed significant improvement (45.50 vs. 2.50, P = 0.000).

Table 3.2: Comparison of cardiac MRI parameters before and after pulmonary valve replacement in patients with repaired tetralogy of Fallot. Data are presented as mean ± SD or median [25th–75th interquartile range]. P, for the Wilcoxen-Rank test. P-value is significant if < 0.05

Parameters		**Before PVR (n=18)**	**After PVR (n=18)**	***P***
Right Ventricle	**EDVI, mL/m^2**	166.50 (143.50–184.00)	115.00 (104.50–125.25)	0.000
	ESVI, mL/m^2	93.00 (81.50–113.75)	65.50 (58.25–69.25)	0.000
	SVI, mL/m^2	67.50 (57.75–71.25)	51.00 (46.75–56.25)	0.001
	EF, %	41.50 (38.75–44.25)	43.50 (40.00–45.25)	0.076
Left Venticle	**EDVI, mL/m^2**	88.00 (81.25–97.25)	82.00 (73.00–92.25)	0.117
	ESVI, mL/m^2	46.00 (40.00–50.25)	41.00 (35.75–47.25)	0.017
	SVI, mL/m^2	42.00 (39.25–51.25)	39.50 (36.75–47.50)	0.341
	EF, %	49.50 (46.5–52.25)	51.00 (48.00–54.25)	0.074
PR fraction, %		45.50 (38.00–52.00)	2.50 (1.00–21.00)	0.000

3.3.2 Atrial and Ventricular Strain Measurements

There was a significant difference in terms of left atrial conduit (9.50 vs. 13.70, P =0.001) and pump (17.05 vs. 18.90, P = 0.006) strains after pulmonary valve replacement. However, no significant change was revealed in the left atrial reservoir strain (0.40 vs. 0.01; P = 0.410). There were no differences in the left atrial reservoir (0.95 vs. 0.90; P = 0.512), conduit (-1.25 vs. -1.30; P = 0.932), and pump (-0.75 vs. -0.75, P = 0.477) strain rate parameters. On the other hand, conduit (6.70 vs 9.80, P =0.004) and pump (14.90 vs. 19.20, P = 0.015) strains for the right atrium showed significant improvement after pulmonary valve replacement. However, no significant change was revealed in terms of right atrial reservoir strain (0.30 vs. 0.42; P = 0.177). Furthermore, there were no differences in the right atrial reservoir (0.90 vs. 1.05; P = 0.512), conduit (-0.90 vs. -1.10; P = 0.125), and pump (-1.10 vs. -1.10, P = 0.484) strain rates. **Table 3.3** shows the atrial strain parameters in the patients with repaired TOF before and after PVR.

There was a significant progression in global left ventricular circumferential (-15.80 vs. -19.45, P = 0.001), longitudinal (-17.75 vs. -18.80, P = 0.043), and radial (26.85 vs. 33.05, P = 0.002) strain parameters after pulmonary valve replacement. A significant progression in right ventricular global circumferential strain was revealed after PVR (-14.25 vs. -16.30, P = 0.007). Furthermore, right ventricular global longitudinal (-18.05 vs. -18.50, P = 0.068) and radial (32.00 vs. 32.95, P = 0.055) strain parameters were unchanged after pulmonary valve replacement. Table 3.4 shows the global strain parameters for the left and right ventricles before and after pulmonary valve replacement.

Table 3. 3: Comparison of atrial strain cardiac MRI parameters before and after pulmonary valve replacement in patients with repaired tetralogy of Fallot. Data are presented as median [25th–75th interquartile range]. P, for the Wilcoxen-Rank test. P-value is significant if < 0.05

	LEFT ATRIUM			**RIGHT ATRIUM**		
	Before PVR (n=18)	**After PVR (n=18)**	*P*	**Before PVR (n=18)**	**After PVR (n=18)**	*P*
GLOBAL LONGITUDINAL STRAIN PARAMETERS						
Reservoir (%)	0.40 (0.01–1.30)	0.01 (0.05–0.40)	0.410	0.30 (0.02–1.85)	0.42 (0.01–0.90)	0.177
Conduit (%)	9.50 (7.20–11.57)	13.70 (11.35– 23.70)	0.001	6.70 (3.80– 9.05)	9.80 (8.60– 14.75)	0.004
Pump (%)	17.05 (12.52–18.67)	18.90 (17.80–24.25)	0.00	14.90 (10.90–18.25)	19.20 (14.20–20.70)	0.015
STRAIN RATE PARAMETERS						
Reservoir strain rate (s^{-1})	0.95 (0.67–.155)	0.90 (070–1.00)	0.512	0.90 (0.65–1.15)	1.05 (0.80–1.35)	0.439
Conduit strain rate (s^{-1})	-1.25 (-1.75– -1.00)	-1.30 (-1.8– -1.20)	0.932	-0.90 (-1.25– -0.50)	-1.10 (-1.48– -0.83)	0.125
Pump strain rate (s^{-1})	-0.75 (-1.13– -0.57)	-0.75 (-1.10– -0.63)	0.477	-1.10 (-1.25–-0.75)	-1.10 (-1.40– -0.95)	0.484

Table 3.4: Comparison of ventricular strain cardiac MRI parameters before and after pulmonary valve replacement in patients with repaired tetralogy of Fallot. Data are presented as median [25th–75th interquartile range]. P, for the Wilcoxen-Rank test. P-value is significant if< 0.05

	LEFT VENTRICLE			**RIGHT VENTRICLE**		
	Before PVR (n=18)	**After PVR (n=18)**	***P***	**Before PVR (n=18)**	**After PVR (n=18)**	***P***
GLOBAL STRAIN PARAMETERS						
Circumferential, %	-15.80 (-17.65– -14.22)	-19.45 (-20.20– -18.32)	0.001	-14.25 (-16.42– -12.75)	-16.30 (-18.52– -14.82)	0.007
Longitudinal, %	-17.50 (-19.20– -12.93)	-18.80 (-19.45– -16.23)	0.043	-18.05 (-18.85– -16.17)	-18.50 (-20.72– -17.82)	0.068
Radial, %	26.85 (22.53–30.00)	33.05 (30.60–36.03)	0.002	32.00 (24.53–34.60)	32.95 (30.78–40.58)	0.055

3.4 Discussion

In this study, we evaluated atrial and ventricular reverse remodeling by feature-tracking cardiac MRI strain technique after transcatheter PVR in patients with repaired TOF. The main findings of this study are 1) a significant increase in global longitudinal conduit and pump strain parameters for left and right atria, 2) a significant increment in the global circumferential strain parameters of the right ventricle, 3) a significant progression of global circumferential, longitudinal, and radial left ventricle strain parameters, and 4) a significant progression of the right ventricle function and cardiac MRI parameters one year after transcatheter pulmonary valve replacement.

Higher conduit and pump strains for left and right atria without significant change in reservoir function after pulmonary valve replacement. A significant decrease in passive strain corresponds to worse left atrial conduit function, which is closely related to left ventricular compliance (Hoit BD 2014).

Increased passive conduit and booster strain might be directly correlated with improved ventricular relaxation (Kowallick JT et al. 2014). The absence of significant alterations in reservoir function despite the observed changes in conduit and pump strains implies that the overall ability of the atria
to store and release blood remains relatively stable (Kowallick JT et al. 2014). This would be explained by the patients who had no severe tricuspid valve regurgitation in our study group, who may suggest a certain degree of compensatory mechanism or resilience in atrial function and compliance following PVR without significant tricuspid valve regurgitation.
In our study, we also observed higher global circumferential, longitudinal, and radial strain of the left ventricle and global circumferential strain of the right ventricle after transcatheter pulmonary valve replacement. However, the right ventricular global longitudinal and radial strain parameters were unchanged. The lack of improvement in the right ventricular global longitudinal and radial strain parameters indices may be because restoration of normal loading conditions occurred after the myocardium had sustained irreversible damage.
In recent years, transcatheter PVR has been an alternative technique in selected patients without right ventricular outflow tract aneurysm or other indications for surgical correction (Gillespie MJ et al. 2012). However, limited studies focusing on the effect of transcatheter PVR on ventricular strain have been designed on the variable characteristics of the right ventricular outflow tract morphology, and initial surgical history is often based on echocardiography-based techniques (Harrild DM et al. 2013; Kutty S et al. 2008; Moiduddin N et al. 2012). In a study by Irwin M. et al., no significant difference was demonstrated regarding right and left ventricle longitudinal and circumferential strain through cardiac MRI after pulmonary valve replacement. Notably, PVR was performed dominantly surgically (almost 58 % of the cohort) (Irwin M et al. 2023). The unchanged or worsened right ventricular in various studies might be attributed to the surgical PVR technique requiring thoracotomy and right ventricle outflow tract transection (Kawakubo M et al. 2021; Sjöberg P et al. 2020). Surgical pulmonary valve replacement, while a standard practice for many years, requires extracorporeal circulation, sternotomy, and right ventricular outflow tract dissection. On the other hand, a study from our group evaluated the strain characteristic of the repaired TOF patients before pulmonary valve implantation and reported that the patients referred to surgical technique had worse ventricular strain

parameters than the transcatheter group (Ozkok S et al. 2023). The lack of improvement in right ventricle strain parameters after the surgical PVR group in the literature would be explained by worse baseline strain parameters before the procedure and the invasive nature of the technique. Similarly, a better response of the left ventricle than the right ventricle may prove, considering that the right ventricle is subject to complications from pulmonary valve disease and multiple surgical procedures (Monti et al. 2020; Tretter JT, Redington AN 2018). The underlying initial anatomy and surgery-related factors may have had unfavorable effects on normal cardiac remodeling. A significant decrease in right ventricle volume without improvement in the right ventricle ejection fraction was found in our study, as expected. Based on the effects of pulmonary valve replacement, previous studies revealed similar results in terms of ventricular volume and function (Buechel ERV et al. 2005; Vliegen HW et al. 2002). Balasubramanian S. et al. found that right ventricle end-diastolic volume, end-systolic volume, and ejection fraction declined, and left ventricle end-diastolic volume and end-systolic volume both increased after surgical pulmonary valve replacement. However, no significant change was revealed in the left ventricle ejection fraction (Balasubramanian S et al. 2018). The common results in these studies are a decrease in right ventricle end-diastolic volume index, with no change in right ventricle and left ventricle ejection fractions (Ferraz Cavalcanti PE et al. 2013; Kutty S et al. 2008; Henkens IR et al. 2007). This study had some limitations that must be highlighted. The retrospective methodology of the research and the small cohorts in the single-center group represents the main limitation. However, all cardiac MRI examinations were performed using an institutionally approved clinical protocol and evaluated by experts in congenital heart disease. In addition, we did not report inter-study reproducibility. Nevertheless, inter-study reproducibility of strain measured by feature-tracking cardiac MRI has been reported In various studies, a satisfactory coefficient of variation and intraclass correlation coefficient were found (Hu L et al. 2021; Kutty S et al. 2008).

In conclusion, transcatheter PVR in patients with repaired TOF leads to significant alterations in atrial and ventricular strain parameters without significant changes in volume and function characteristics. Feature-tracking cardiac MRI strain analyses applied to standard cine images without performing additional time-consuming sequences would be included in the repaired tetralogy of the Fallot imaging protocol.

Chapter 4

4 COMPUTATIONAL MODELING FOR PATIENT SPECIFIC SURGICAL PLANNING TO ACHIEVE OPTIMAL PULMONARY ARTERY FLOW AFTER FONTAN SURGERY

4.1 Introduction

The Fontan procedure serves as a palliative treatment for pediatric patients with functionally single ventricle congenital heart disease, which occurs in approximately 0.08 to 0.4 per 1,000 live births (van der Ven J.P.G et al 2018). The Fontan procedure, also known as the total cavopulmonary connection (TCPC), was first described in 1971 as a total right heart bypass for tricuspid atresia. In the Fontan operation, the superior vena cava is directly anastomosed to the pulmonary artery, and the inferior vena cava is also routed to the pulmonary artery through a conduit created within a baffle, a technique known as the lateral tunnel approach. The approach involves a series of staged procedures developed more recently to connect systemic venous return directly to the pulmonary circulation, provided pulmonary pressures are low. This effectively enables the systemic venous circulation to bypass the heart (Fontan F and Baudet E, 1971).

Over the past four decades, the Fontan operation has been implemented as a surgical treatment for patients with tricuspid atresia and has evolved into a groundbreaking therapy for those with univentricular heart physiology. The Fontan completion procedure is typically performed in childhood for various congenital heart defects, including tricuspid atresia, hypoplastic left heart syndrome (the most common), hypoplastic right heart syndrome, pulmonary atresia with an intact ventricular septum, double-inlet left ventricle, double outlet right ventricle, unbalanced atrioventricular canal defects, Ebstein's anomaly suitable for Fontan correction, and congenitally corrected transposition of the great arteries. The success of the procedure relies on optimal physiological and anatomical conditions, such as good ventricular function, normal pulmonary vascular resistance, and adequately sized pulmonary arteries (Attard C et al. 2018).

Despite the lifesaving efficacy of the Fontan procedure for single-ventricle patients, there is an increasing incidence of complications in the long-term postoperative period. Complications following the Fontan procedure are common and are primarily associated with increased venous pressure, congestion, and chronic low cardiac output. These complications include early and late mortality, mild to moderate exercise intolerance, residual cardiomegaly, ventricular dysfunction, rhythm and conduction disturbances, hepatomegaly, lymphatic dysfunction leading to protein-losing enteropathy, systemic venous thrombi, ascites, and peripheral edema (Gewillig M. 2005). For successful single-ventricle palliation in both the short and long term, healthy pulmonary circulation, both anatomically and physiologically, is crucial. Branch pulmonary artery stenosis in patients with single-ventricle physiology is often surgically corrected with excellent outcomes (Kim H.K et al. 2006). Numerous experimental and clinical studies have aimed to deepen the understanding of Fontan circulation, leading to several modifications of the procedure and improved patient outcomes (Baretta et al. 2011; Fogel, Khiabani, and Yoganathan 2013; Siallagan et al. 2018; Trusty, Slesnick, et al. 2018; Trusty et al. 2019; van Bakel et al. 2018). Nevertheless, challenges associated with Fontan circulation attrition persist, with concerns such as elevated systemic venous pressure, increased pulmonary artery resistance, reduced preload, and increased afterload remaining significant issues (Kanakis MA et al. 2009).

Serious long-term complications are inevitable following Fontan surgery in patients with single-ventricle physiology. To achieve optimal outcomes in the long run, ensuring a balanced distribution of hepatic flow to both lungs in pulmonary flow is crucial. This chapter aims to assess pulmonary flow distribution by applying a patient-specific surgical approach via CFD modeling.

4.2 Materials and Methods

4.2.1 Patient groups and data collection

A cohort of fourteen patients (M/F: 5/9), aged 2 to 28 years, with single ventricle physiology, were recruited for this study. Three-dimensional pre-surgical anatomical reconstructions, including key surgical landmarks such as the ventricle, aorta, and hepatic veins, were performed. Body surface area was between 0.3 and 2.19 m^2. Seven patients had bilateral SVC. Patients were recruited sequentially, as shown in **Table 4.1**, with no exclusion criteria for those regularly listed for surgery.

Table 4.1 Demographic data of the patient cohort, information about the tested virtual surgery configurations.

Patient	Age	Sex	BSA	Bilateral SVC	Number of surgical alternatives simulated	Selected graft type
1	6	M	1.1	Yes	9	Y-graft
2	14	F	1.2	Yes	3	Y-graft
3	11	M	1.19	No	6	Y-graft
4	13	F	1.3	Yes	4	Y-graft
5	18	F	1.4	Yes	5	Y-graft
6	7	F	0.7	No	3	Y-graft
7	9	F	1.2	No	9	Hep-to Azy
8	6	M	0.4	No	3	Extra-cardiac
9	2	F	0.3	No	4	Extra-cardiac
10	14	M	1.32	Yes	11	Intra-cardiac
11	3	F	0.7	No	11	Intra-cardiac
12	28	F	1.76	Yes	5	Extra-cardiac
13	12	F	1.11	Yes	5	Y-graft
14	26	M	2.19	No	7	Extra-cardiac

4.2.2 Cardiac Magnetic Resonance Imaging

Pre-surgical three-dimensional anatomy, phase-contrast cardiac magnetic resonance imaging (MRI) flow boundary conditions, and cardiac catheterization data are used to estimate resistance boundary conditions specified downstream of the pulmonary arteries. Post-operative MRI scans were conducted to verify the computational fluid dynamics (CFD) models for the recruited patients.

All cardiac MRI examinations were performed using a 1.5-Tesla scanner with a 32-channel phased-array abdominal coil with electrocardiographic gating. No sedation was required during the examination. A cine-steady state-free precession sequence of two-chambers, four-chambers, and short-axis views was revealed for all patients. Image slices were acquired during one breath-hold of 12 seconds with retrospective gating and 20 cardiac phases. A 0.2 mmol/kg gadolinium-based contrast agent was performed for static magnetic resonance angiography. Contrast-enhanced magnetic resonance angiography (MRA) was used to prescribe the phase-contrast imaging of the branch pulmonary arteries, ascending and descending aorta, pulmonary veins, and superior and inferior vena cava. The optimal velocity encoding value of the pulmonary artery was calculated by the calculation Bernoulli equation reported gradients in the echocardiography report. Venc value was applied as 120 cm/sec for the aorta and 80 cm/sec for pulmonary and systemic veins.

The raw image data of the contrast-enhanced MRA was processed by medical image processing software Mimics Innovation Suite 17 (Materialise, Leuven, Belgium) and 3D Slicer open-source application for segmentation of the region of interest. The heart cavity and aorta were also included in the pre-surgery models to provide landmarks for surgical planning.

For post-operative verification of the intended surgical template, patients underwent MRA scanning within one year of surgery using the same protocol. Flow conditions were measured using the diagnostic catheter angiography gradients of the patient. In post-operative models, the left and right pulmonary artery (LPA and RPA), inferior vena cava (IVC), hepatic vein (HEP), and superior vena cava (SVC) were reconstructed.

4.2.3 Computational fluid dynamics

The models were analyzed using CFD techniques, which provided detailed 3D flow fields, lung perfusions, pressure drops, and hydrodynamic power losses. This analysis begins with the creation of an idealized model geometry, either designed within a computer-aided design package or reconstructed from cardiac MRI patient data. The next step involves grid generation, where the vessel volume is divided into thousands of smaller computational elements or grids/meshes. At each element, the governing conservation equations of mass and momentum for blood flow are solved. Although the mathematical framework for blood flow does not involve assumptions, achieving a credible numerical solution to these equations requires careful specification of boundary conditions, thorough global and local mesh verification studies, and in vitro experimental validation.

The CFD simulation methodology employed in this study was consistent with the approach used in previous research focused on Fontan patients (Pekkan K et. al 2005 and Yoshida M et. al 2013). Technical details of the material and method are available from a previous study by the same group (Lashkarinia S.S. et al. 2022).

Patients were regularly followed up postoperatively for oxygen saturation levels in 1-year postoperative follow-up. The results were compared via statistical analysis.

4.3 Results

There was no mortality in our cohort. Statistical analysis revealed a significant increase in postoperative oxygen saturation values (means of 78% and 91% pre- and postoperatively, respectively) ($p < 0.05$). The increase in mean hepatic flow for the left and right pulmonary artery (LPA/RPA) was also statistically significant ($p < 0.05$). The deviation from the targeted 50/50 hepatic flow distribution postoperatively between the best and worst alternatives was statistically significant (± 14% and 42%, respectively) ($p < 0.05$). Pre- and postoperative hepatic flow splits from computational fluid dynamics simulations and clinically measured pre- and postoperative oxygen saturation levels are presented in Table 4.2.

Table 4.2 Pre-and postoperative hepatic flow splits from computational fluid dynamics simulations and clinically measured pre- and postoperative oxygen saturation levels. Pre-surgery hepatic flow is the part that is delivered to the lungs.

Patient	Hepatic Flow Distribution (%LPA/RPA)			Power Loss(mW)		Pulmonary Flow Distribution (%LPA/RPA)			Oxygen Saturation(%)	
	Pre-Op	Best (Post-Op)	Worst	Best	Worst	Pre-Op	Best (Post-Op)	Worst	Pre-Op	Post-Op
1	15/31	31/69	90/10	30	28	22/78	44/56	47/53	73	91
2	0/100	38/62	0/100	65	26	51/49	53/47	51/49	74	93
3	0/0	33/67	100/0	48	52	81/19	80/20	71/29	80	89
4	27/2	27/73	17/83	5.87	4.27	71/29	60/40	59/41	79	92
5	7/5	39/61	100/0	69	70	36/64	53/47	55/45	80	92
6	0/46	55/45	2/98	29.8	16.3	40/60	36/64	35/65	75	89
7	40/36	43/57	100/0	13.5	4.8	56/44	52/48	53/47	88	96
8	-	67/33	92/8	11.7	12	-	46/54	47/52	90	95
9	-	50/50	0/100	26	12.9	-	48/52	41/59	87	94
10	18/21	63/37	87/13	3.03	11.3	27/13	61/39	65/35	75	84
11	5/10	55/45	100/0	32.81	44.01	39/14	69/31	62/38	73	90
12	54/46	82/18	93/7	7.97	5.95	12/88	40/60	39/61	72	86
13	0/0	37/63	25/75	7.6	6.2	62/38	54/46	53/47	75	90
14	24/2	29/71	83/17	7.2	12.45	50/50	51/49	50/50	70	90

4.3.1 Total and hepatic flow distribution

Hemodynamic pre-surgery simulations indicated that 38 % of the HEP flow bypassed the lungs and went directly to the aorta. It was predicted that the LPA received only 29 % of the total HEP flow (**Figure 4.1A**) before surgery. The total venous flow in the selected virtual surgery model was predicted to be more balanced, with 65 % directed to the LPA and 35 % to the RPA (**Figure 4.1B**). In the actual post-surgery model, the total venous flow split to the left lung through the venous flow was 65 % and 35 % to the RPA (**Figure 4.1C**). The predicted HEP flow split to the lungs closely matched the post-surgery model in terms of anatomy and clinical results, with a prediction error of less than 3% (**Figure 4.2E**). The efficacy of the surgery was confirmed in a postoperative cardiac MRI conducted approximately one year later. It can be inferred that total venous flow to the LPA increased as well. Consequently, the underdeveloped LPA observed in pre-surgery scans was able to grow effectively, leading to a balanced size between the LPA and RPA, as recorded in postoperative data (**Figure 4.1C and 4.1F).**

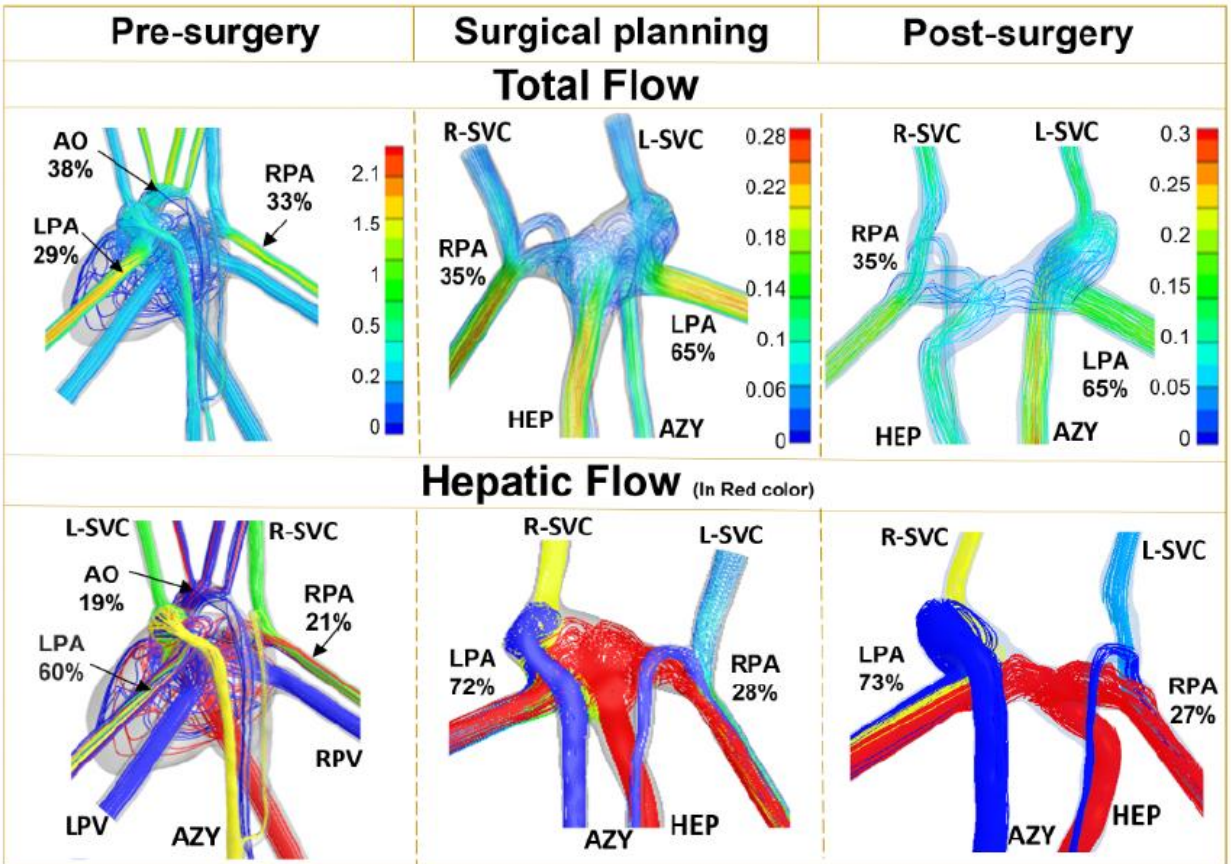

Figure 4.1: Computational fluid dynamics simulations of (A, D) pre-surgery, (B, E) selected surgical alternative, and (C, F) post-surgery model. The first row shows the streamlines of inflows in different colors (A–C). The hepatic flow split is shown in red color. The second row indicates the velocity streamlines and total venous flow splits to the lungs (D–F). Quantified flow splits to the lungs are reported in percentages.

4.4 Discussion

In the present study, we evaluated the efficacy of Fontan surgery in terms of branch pulmonary artery flow distribution, which was confirmed in postoperative cardiac MRI approximately one year later.

The Fontan procedure has been pivotal in the surgical management of single-ventricle congenital heart defects, yet long-term complications related to Fontan circulation remain a significant concern. Ensuring optimal pulmonary artery flow post-Fontan is crucial to improving patient outcomes, and computational modeling has emerged as a promising tool for patient-specific surgical planning.

We showed that the use of CFD in pre-surgical planning and patient-specific models can accurately predict postoperative flow dynamics. The Fontan procedure, by redirecting venous blood directly to the pulmonary arteries bypassing the heart, relies heavily on the balance and distribution of blood flow to maintain adequate oxygenation levels. CFD simulations can be used to predict and optimize blood flow patterns, aiming to reduce energy losses and ensure even distribution of oxygen-rich blood to both lungs.

Studies have shown that uneven hepatic flow distribution, a common issue in TCPC, can lead to complications such as pulmonary arteriovenous malformations, which can significantly reduce blood oxygen saturation (Srivastava D et al. 1995; Duncan BW and Desai S, 2003). By utilizing patient-specific modeling, surgeons can preoperatively simulate different surgical strategies to minimize the risk of PAVMs and other complications that contribute to low oxygen saturation.

Frieberg P et al. explore the relationship between hepatic and pulmonary blood flow and its impact on pulmonary flow, pulmonary vascular resistance, and oxygen saturation in Fontan patients (Frieberg P et al., 2023). Using cardiac MRI data and patient-specific CFD models, they found that the hepatic-to-pulmonary blood flow balance significantly correlates with pulmonary vein flow, pulmonary vascular resistance, and oxygen saturation. The study also demonstrated the clinical applicability of these findings in a case study, suggesting that cardiac MRI combined with CFD could aid in planning surgical and interventional procedures for Fontan patients.

The feasibility of this approach is confirmed by the successful implementation in a clinical setting for achieving optimal hemodynamic outcomes on a case-by-case basis. In both previous (Lashkarinia SS et al. 2022) and the current study, surgical planning simulations have shown the effectiveness of achieving optimal patient-specific hemodynamics, such as power loss, hepatic flow distribution, and pulmonary flow distribution, significantly improving the patient's exercise capability and oxygen saturation levels and quality of life.

In conclusion, despite the complex long-term vascular growth and remodeling typical in Fontan patients, the computational hemodynamic predictions align well with the in vivo postoperative measurements observed in this patient cohort. Virtual surgical simulations have proven effective in achieving precise patient-specific optimization of hepatic flow split and pulmonary perfusion, leading to notably better postoperative oxygen saturation levels. The proposed template is recommended for adoption due to its clinical benefits and its natural emergence from an unbiased pre-surgical computational customization process. Given the variability in patient anatomy and flow rates, computational pre-surgical customization is advised for any surgical template to ensure optimal hemodynamics.

Chapter 5

5 CONCLUSION and FUTURE WORKS

This thesis explores the novel cardiac MRI sequences used for the evaluation of morphological and myocardial distortion changes in patients with tetralogy of Fallot and flow distribution in patients with single-ventricle physiology. Cine, 2D phase contrast, and MRA sequences are used for the assessment of myocardial distortion evaluation, 3D printing, and CFD analysis.

In the first part of the thesis, the study explores the differences in functional and 3D morphological characteristics of the right ventricular outflow tract and branch pulmonary arteries between surgical and transcatheter pulmonary valve replacement in patients with repaired tetralogy of Fallot. It was found that circumferential and radial magnetic resonance imaging strain decreased in the surgical-pulmonary valve replacement group, while the transcatheter-pulmonary valve replacement group had smaller left pulmonary artery diameters but higher branch pulmonary artery flow and diameter ratios. Significant correlations were identified between right ventricular outflow tract types and specific cardiac parameters. Additionally, integrating 3D printing of patient-specific models could enhance preprocedural planning by providing detailed anatomical visualization, potentially supporting the choice of the more suitable pulmonary valve replacement approach. The study's findings underscore the importance of 3D modeling in evaluating the right ventricular outflow tract for patients with surgically corrected tetralogy of Fallot. By integrating 3D printing of patient-specific models, clinicians can achieve a detailed and accurate representation of the right ventricular outflow tract and branch pulmonary arteries, which is crucial for preprocedural planning. This enhanced visualization allows for better assessment of anatomical variations and potential challenges, thereby supporting more precise decision-making between surgical and transcatheter pulmonary valve replacement approaches. The use of 3D models can improve surgical planning, predict outcomes, and tailor interventions to individual patient anatomy, ultimately contributing to better treatment outcomes and personalized care.

The second part focuses on atrial and ventricular strain changes post-pulmonary valve replacement, showing significant improvements in ventricular function and atrial strain, particularly in the left ventricle. Results showed significant improvements in right ventricular function and volume and in global longitudinal conduit and pump strain for both atria. Significant increases were also observed in the global circumferential, longitudinal, and radial strain of the left ventricle and the circumferential strain of the right ventricle, while other strain parameters for the right ventricle remained unchanged. This study addresses a critical gap in understanding the effects of transcatheter pulmonary valve replacement on myocardial strain in patients with repaired tetralogy of Fallot. The findings suggest that adding strain analysis to routine cardiac MRI protocols could enhance patient management without requiring additional imaging sequences, thereby offering a more comprehensive assessment of heart function in these patients. This study underscores the importance of incorporating advanced imaging techniques to optimize treatment outcomes in this population. This study is crucial because it fills a significant knowledge gap by examining the impact of transcatheter pulmonary valve replacement on atrial and ventricular strain in patients with surgically corrected tetralogy of Fallot.

The third part focuses on the long-term complications following the Fontan procedure in patients with single-ventricle physiology, particularly pulmonary flow distribution and post-operative oxygen saturation. While pre-surgical planning can improve hemodynamic performance and outcomes, there is no quantitative experimental validation of hepatic flow distribution. This gap raises concerns about the predictive accuracy of current computational simulations used in pre-surgical planning for these patients.

Building on the findings of this thesis, future research could explore several key areas to further advance the evaluation and management of congenital heart disease using cardiac MRI. One potential direction is the development and validation of more refined computational models that integrate patient-specific data from 4D flow MRI and CFD simulations. These models could improve the predictive accuracy of hemodynamic outcomes, particularly in complex cases such as single-ventricle physiology and post-Fontan patients. Additionally, expanding the use of 3D printing and virtual reality in pre-surgical planning could enhance the precision of interventions by allowing surgeons to interact with detailed, patient-specific anatomical models in a simulated environment. Research could also focus on optimizing MRI sequences to reduce scan times and improve patient comfort, making these advanced imaging techniques more accessible in routine clinical practice. Finally, longitudinal studies are needed to assess the long-term impact of transcatheter pulmonary valve replacement on myocardial function, particularly in relation to strain parameters, and to determine the most effective follow-up protocols for these patients. These efforts would contribute to a more personalized approach to managing congenital heart disease, ultimately improving patient outcomes.

In addition, the methodologies and insights from this thesis can be further expanded by leveraging our group’s previous work. Notably, our earlier studies on Fontan patients, including the development of a novel Fontan Y-graft for interrupted inferior vena cava and azygos continuation (Lashkarinia et al., 2022), have laid the groundwork for refining CFD simulation techniques. These studies demonstrated the potential of CFD models to predict post-surgical hemodynamic outcomes, emphasizing the need for continued refinement and validation of these techniques in future research. Further exploration in this direction will help in advancing the understanding of complex congenital heart conditions and optimizing treatment strategies.

Bibliography

Anwar, S., Harris, M. A., Whitehead, K. K., et al. (2017). The impact of the right ventricular outflow tract patch on right ventricular strain in tetralogy of Fallot: A comparison with valvar pulmonary stenosis utilizing cardiac magnetic resonance. Pediatric Cardiology, 38, 617–623.

Attard, C., Huang, J., Monagle, P., & Ignjatovic, V. (2018). Pathophysiology of thrombosis and anticoagulation post Fontan surgery. Thrombosis research, 172, 204–213.

Babu-Narayan, S. V., Kilner, P. J., Li, W., et al. (2006). Ventricular fibrosis suggested by cardiovascular magnetic resonance in adults with repaired tetralogy of Fallot and its relationship to adverse markers of clinical outcome. Circulation, 113, 405–413.

Baretta, Alessia, Chiara Corsini, Weiguang Yang, Irene E Vignon-Clementel, Alison L Marsden, Jeffrey A Feinstein, T-Y Hsia, Gabriele Dubini, Francesco Migliavacca, and Giancarlo Pennati. 2011. 'Virtual surgeries in patients with congenital heart disease: a multi-scale modelling test case', Philosophical Transactions of the Royal Society A: Mathematical, Physical and Engineering Sciences, 369: 4316-30.

Baumgartner, H., De Backer, J., Babu-Narayan, S. V., et al. (2021). 2020 ESC guidelines for the management of adult congenital heart disease. European Heart ournal, 42, 563-645.

Boshoff, D. E., Cools, B. L., Heying, R., et al. (2013). Off-label use of percutaneous pulmonary valved stents in the right ventricular outflow tract: Time to rewrite the label? Catheterization and Cardiovascular Interventions, 81, 987-995.

Buechel, E. R. V., Grosse-Wortmann, L., Fratz, S., et al. (2015). Indications for cardiovascular magnetic resonance in children with congenital and acquired heart disease: An expert consensus paper of the Imaging Working Group of the AEPC and the Cardiovascular Magnetic Resonance Section of the EACVI. Eur Heart J Cardiovasc Imaging, 16(3), 281-297.

Chung, R., & Taylor, A. M. (2014). Imaging for preintervention planning: transcatheter pulmonary valve therapy. Circulation. Cardiovascular imaging, 7(1), 182–189.

Dandel, M., Lehmkuhl, H., Knosalla, C., et al. (2009). Strain and strain rate imaging by echocardiography – Basic concepts and clinical applications. Current Cardiology Reviews, 5, 133–148.

Davlouros, P. A., Kilner, P. J., Hornung, T. S., et al. (2002). Right ventricular function in adults with repaired tetralogy of Fallot assessed with cardiovascular magnetic resonance imaging: Detrimental role of right ventricular outflow aneurysms or akinesia and adverse right-to-left ventricular interaction. Journal of the American College of Cardiology, 40, 2044–2052.

Dillman, J. R., Hernandez, R. J. (2017). Role of CT in the evaluation of congenital cardiovascular disease in children. American Journal of Roentgenology, 192(5), 1219-1231.

Duncan, B. W., & Desai, S. (2003). Pulmonary arteriovenous malformations after cavopulmonary anastomosis. The Annals of thoracic surgery, 76(5), 1759–1766. https://doi.org/10.1016/s0003-4975(03)00450-8

Ferrari, I., Shehu, N., Mkrtchyan, N., et al. (2020). Different CMR imaging modalities for native and patch-repaired right ventricular outflow tract sizing: Impact on percutaneous pulmonary valve replacement planning. Pediatric Cardiology, 41, 382–388.

Ferraz Cavalcanti, P. E., Sá, M. P., Santos, C. A., et al. (2013). Pulmonary valve replacement after operative repair of tetralogy of Fallot: Meta-analysis and meta-regression of 3,118 patients from 48 studies. Journal of the American College of Cardiology, 62, 2227-2243. https://doi.org/10.1016/j.jacc.2013.04.107

Fogel, Mark A, Reza H Khiabani, and Ajit Yoganathan. 2013. 'Imaging for preintervention planning: pre-and post-Fontan procedures', Circulation: Cardiovascular Imaging, 6: 1092-101.

Fontan, F., & Baudet, E. (1971). Surgical repair of tricuspid atresia. Thorax, 26(3), 240–248. https://doi.org/10.1136/thx.26.3.240

Fratz, S., Chung, T., Greil, G. F., Samyn, M. M., Taylor, A. M., Valsangiacomo Buechel, E. R., & Powell, A. J. (2013). Guidelines and protocols for cardiovascular magnetic resonance in children and adults with congenital heart disease: SCMR expert consensus group on congenital heart disease. Journal of Cardiovascular Magnetic Resonance, 15(1), 1-26.

Frieberg, P., Sjöberg, P., Hedström, E., Carlsson, M., & Liuba, P. (2023). In vivo hepatic flow distribution by computational fluid dynamics can predict pulmonary flow distribution in patients with Fontan circulation. Scientific reports, 13(1), 18206. https://doi.org/10.1038/s41598-023-45396-6

Gatzoulis, M. A., Balaji, S., Webber, S. A., et al. (2000). Risk factors for arrhythmia and sudden cardiac death late after repair of tetralogy of Fallot: A multicenter study. The Lancet, 356, 975–981.

Geva, T. (2013). Indications for pulmonary valve replacement in repaired tetralogy of Fallot: The quest continues. Circulation, 128, 1855–1857.

Gewillig M. (2005). The Fontan circulation. Heart (British Cardiac Society), 91(6), 839–846. https://doi.org/10.1136/hrt.2004.051789

Gillespie, M. J., Rome, J. J., Levi, D. S., et al. (2012). Melody valve implant within failed bioprosthetic valves in the pulmonary position: A multicenter experience. Circulation: Cardiovascular Interventions, 5, 862-870.

Ginat, D. T., Fong, M. W., Tuttle, D. J., Hobbs, S. K., & Vyas, R. C. (2011). Cardiac imaging: Part 1, MR pulse sequences, imaging planes, and basic anatomy. American Journal of Roentgenology, 197(4), 808-815.

Harrild DM, Marcus E, Hasan B et al (2013) Impact of transcatheter pulmonary valve replacement on biventricular strain and synchrony assessed by cardiac magnetic resonance feature tracking. Circ Cardiovasc Interv 6:680–7

Harris, M. A., Whitehead, K. K., Gillespie, M. J., et al. (2011). Differential branch pulmonary artery regurgitant fraction is a function of differential pulmonary arterial anatomy and pulmonary vascular resistance. Journal of the American College of Cardiology: Cardiovascular Imaging, 4, 506–513.

Hasselberg NE, Kagiyama N, Soyama Y et al (2021) The prognostic value of right atrial strain imaging in patients with precapillary pulmonary hypertension. J Am Soc Echocardiogr 34:851–861.e1.

Henkens IR, van Straten A, Schalij MJ et al (2007) Predicting outcome of pulmonary valve replacement in adult tetralogy of Fallot patients. Ann Thorac Surg 83:907–911

Hennein, H. A., Mosca, R. S., Urcelay, G., et al. (1995). Intermediate results after complete repair of tetralogy of Fallot in neonates. Journal of Thoracic and Cardiovascular Surgery, 109, 332–344.

Hickey, E. J., Veldtman, G., Bradley, T. J., et al. (2009). Late risk of outcomes for adults with repaired tetralogy of Fallot from an inception cohort spanning four decades. European Journal of Cardiothoracic Surgery, 35, 156–164.

Hoit B. D. (2014). Left atrial size and function: role in prognosis. Journal of the American College of Cardiology, 63(6), 493–505. https://doi.org/10.1016/j.jacc.2013.10.055

Hu L, Ouyang R, Liu X et al (2021) Impairment of left atrial function in pediatric patients with repaired tetralogy of Fallot: a cardiovascular magnetic resonance imaging study. Int J Cardiovasc Imaging 37:3255-3267.

Irwin M, Reynolds L, Binney G et al (2023) Right Heart Remodeling After Pulmonary Valve Replacement in Patients With Pulmonary Atresia or Critical Stenosis With Intact Ventricular Septum. J Am Heart Assoc 7;12:e031090

Kanakis, M. A., Petropoulos, A. C., & Mitropoulos, F. A. (2009). Fontan operation. Hellenic journal of cardiology : HJC = Hellenike kardiologike epitheorese, 50(2), 133–141.

Kawakubo M, Yamasaki Y, Toyomura D et al (2021) Unchanged right ventricular strain in repaired tetralogy of Fallot after pulmonary valve replacement with radial long-axis cine magnetic resonance images. Sci Rep 23;11:18879

Kessler Iglesias, C., Pouliopoulos, J., Thomas, L., Hayward, C. S., Jabbour, A., & Fatkin, D. (2023). Atrial cardiomyopathy: Current and future imaging methods for assessment of atrial structure and function. Frontiers in cardiovascular medicine, 10, 1099625. https://doi.org/10.3389/fcvm.2023.1099625

Kilner, P. J., Geva, T., Kaemmerer, H., Trindade, P. T., Schwitter, J., & Webb, G. D. (2010). Recommendations for cardiovascular magnetic resonance in adults with congenital heart disease from the respective working groups of the European Society of Cardiology. European Heart Journal, 31(7), 794-805.

Kim, H. K., Kim, W. H., Kim, S. C., Lim, C., Lee, C. H., & Kim, S. J. (2006). Surgical strategy for pulmonary coarctation in the univentricular heart. European journal of cardio-thoracic surgery : official journal of the European Association for Cardio-thoracic Surgery, 29(1), 100–104. https://doi.org/10.1016/j.ejcts.2005.10.032

Kowallick JT, Kutty S, Edelmann F et al (2014) Quantification of left atrial strain and strain rate using Cardiovascular Magnetic Resonance myocardial feature tracking: a feasibility study. J Cardiovasc Magn Reson 16:60 https://doi.org/10.1186/s12968-014-0060-6.

Kutty S, Deatsman SL, Russell D et al (2008) Pulmonary valve replacement improves but does not normalize right ventricular mechanics in repaired congenital heart disease: a comparative assessment using velocity vector imaging. J Am Soc Echocardiogr 21:1216–1221 https://doi.org/10.1016/j.echo.2008.08.009.

Lashkarinia, S. S., Cicek, M., Kose, B., Rezaeimoghaddam, M., Yılmaz, E. H., Aydemir, N. A., Rasooli, R., Ozkok, S., Yurtseven, N., Erdem, H., Pekkan, K., & Sasmazel, A. (2022). A novel Fontan Y-graft for interrupted inferior vena cava and azygos continuation. Interactive cardiovascular and thoracic surgery, 34(6), 1095–1105. https://doi.org/10.1093/icvts/ivac001

Latus H, Born D, Shehu N et al (2021) Favorable Atrial Remodeling After Percutaneous Pulmonary Valve Implantation and Its Association With Changes in Exercise Capacity and Right Ventricular Function. J Am Heart Assoc 19;10:e021416. https://doi.org/10.1161/JAHA.121.021416

Liu, D., Lau, I., Xu, L., Fan, Z., & Sun, Z. (2018). Clinical value of patient-specific three-dimensional printing of congenital heart disease: Quantitative and qualitative assessments. PLoS ONE, 13(2), e0194333.

Luijten, L. W., van den Bosch, E., Duppen, N., Tanke, R., Roos-Hesselink, J., Nijveld, A., van Dijk, A., Bogers, A. J., van Domburg, R., & Helbing, W. A. (2015). Long-term outcomes of transatrial-transpulmonary repair of tetralogy of Fallot. European journal of cardio-thoracic surgery : official journal of the European Association for Cardio-thoracic Surgery, 47(3), 527–534.

Ma, X. J., Tao, L., Chen, X., Li, W., Peng, Z. Y., Jin, J., Zhang, X. L., Xiong, Q. F., Zhong, Z. L., & Chen, X. F. (2015). Clinical application of three-dimensional reconstruction and rapid prototyping technology of multislice spiral computed tomography angiography for the repair of ventricular septal defect of tetralogy of Fallot. Genetics and Molecular Research, 14(1), 1301-1309.

Maceira, A. M., Tuset-Sanchis, L., López-Garrido, M., et al. (2018). Feasibility and reproducibility of feature-tracking-based strain and strain rate measures of the left ventricle in different diseases and genders. Journal of Magnetic Resonance Imaging, 47, 1415–1425.

Markl, M., Schnell, S., Wu, C., Bollache, E., Jarvis, K., Barker, A. J., Robinson, J. D., & Rigsby, C. K. (2016). Advanced flow MRI: emerging techniques and applications. Clinical radiology, 71(8), 779–795.

McElhinney, D. B., Parry, A. J., Reddy, V. M., et al. (1998). Left pulmonary artery kinking caused by outflow tract dilatation after transannular patch repair of tetralogy of Fallot. Annals of Thoracic Surgery, 65, 1120–1126.

Meca Aguirrezabalaga, J. A., Silva Guisasola, J., Díaz Méndez, R., et al. (2020). Pulmonary regurgitation after repaired tetralogy of Fallot: Surgical versus percutaneous treatment. Annals of Translational Medicine, 8, 967.

Moceri, P., Duchateau, N., Gillon, S., et al. (2021). Three-dimensional right ventricular shape and strain in congenital heart disease patients with right ventricular chronic volume loading. European Heart Journal Cardiovascular Imaging, 22, 1174–1181.

Moiduddin N, Texter KM, Cheatham JP et al (2012) Strain echocardiographic assessment of ventricular function after percutaneous pulmonary valve implantation. Congenit Heart Dis 7:361–371. https://doi.org/10.1111/j.1747-0803.2012.00680.x.

Mongeon FP, Ben Ali W, Khairy P et al (2019) Pulmonary Valve Replacement for Pulmonary Regurgitation in Adults With Tetralogy of Fallot: A Meta-analysis-A Report for the Writing Committee of the 2019 Update of the Canadian Cardiovascular Society Guidelines for the Management of Adults With Congenital Heart Disease. Can J Cardiol 35:1772-1783.

Monti CB, Secchi F, Capra D et al (2020) Right ventricular strain in repaired Tetralogy of Fallot with regards to pulmonary valve replacement. Eur J Radiol 131:109235 https://doi.org/10.1016/j.ejrad.2020.109235. Epub 2020 Aug 28.

Negishi, K., Negishi, T., Hare, J. L., et al. (2013). Independent and incremental value of deformation indices for prediction of trastuzumab-induced cardiotoxicity. Journal of the American Society of Echocardiography, 26, 493–498.

Orwat, S., Diller, G. P., Kempny, A., et al. (2016). Myocardial deformation parameters predict outcome in patients with repaired tetralogy of Fallot. Heart, 102, 209–215.

Oshinski JN, Parks WJ, Markou CP, et al (1996) Improved measurement of pressure gradients in aortic coarctation by magnetic resonance imaging. J Am Coll Cardiol 28:1818-26.

Ou-Yang, W. B., Qureshi, S., Ge, J. B., et al. (2020). Multicenter comparison of percutaneous and surgical pulmonary valve replacement in large RVOT. Annals of Thoracic Surgery, 110, 980–987.

Ozkok, S., Ciftci, H. O., Kose, K. B., Yucel, I. K., Sasmazel, A., Celebi, A., & Pekkan, K. (2023). Surgical and transcatheter pulmonary valve replacement in patients with repaired tetralogy of Fallot: cardiac magnetic resonance imaging characteristics and morphology of right ventricular outflow tract. Pediatric radiology, 53(9), 1863–1873.

Pushparajah, K., Duong, P., Mathur, S., & Babu-Narayan, S. (2019). EDUCATIONAL SERIES IN CONGENITAL HEART DISEASE: Cardiovascular MRI and CT in congenital heart disease. Echo research and practice, 6(4), R121–R138. Advance online publication.

Pekkan, K., Kitajima, H. D., de Zélicourt, et. al (2005). Total cavopulmonary connection flow with functional left pulmonary artery stenosis. Circulation, 112(21), 3264–3271.

Scatteia A, Baritussio A, Bucciarelli-Ducci C (2017) Strain imaging using cardiac magnetic resonance. Heart Fail Rev 22:465-476. https://doi.org/10.1007/s10741-017-9621-8

Schievano, S., Coats, L., Migliavacca, F., et al. (2007). Variations in right ventricular outflow tract morphology following repair of congenital heart disease: Implications for percutaneous pulmonary valve implantation. Journal of Cardiovascular Magnetic Resonance, 9, 687–695.

Shen, W. C., Chen, C. A., Chang, C. I., et al. (2020). Outflow tract geometries are associated with adverse outcome indicators in repaired tetralogy of Fallot. Journal of Thoracic and Cardiovascular Surgery, 162, 196–205.

Siallagan, Dominik, Yue-Hin Loke, Laura Olivieri, Justin Opfermann, Chin Siang Ong, Diane de Zélicourt, Anastasios Petrou, Marianne Schmid Daners, Vartan Kurtcuoglu, and Mirko Meboldt. 2018. 'Virtual surgical planning, flow simulation, and 3-dimensional electrospinning of patient-specific grafts to optimize Fontan hemodynamics', The Journal of thoracic and cardiovascular surgery, 155: 1734-42.

Sjöberg P, Ostenfeld E, Hedström E et al (2020) Changes in left and right ventricular longitudinal function after pulmonary valve replacement in patients with Tetralogy of Fallot. Am J Physiol Heart Circ Physiol 318:H345-H353 https://doi.org/10.1152/ajpheart.00417.2019.

Srivastava, D., Preminger, T., Lock, J. E., Mandell, V., Keane, J. F., Mayer, J. E., Jr, Kozakewich, H., & Spevak, P. J. (1995). Hepatic venous blood and the development of pulmonary arteriovenous malformations in congenital heart disease. Circulation, 92(5), 1217–1222. https://doi.org/10.1161/01.cir.92.5.1217

Stout, K K., Daniels, C. J., Aboulhosn, J. A., et al. (2019). 2018 AHA/ACC guideline for the management of adults with congenital heart disease: Executive summary: A report of the American College of Cardiology/American Heart Association task force on clinical practice guidelines. Journal of the American College of Cardiology, 73, 1494–1563.

Sutton, N. J., Peng, L., Lock, J. E., et al. (2008). Effect of pulmonary artery angioplasty on exercise function after repair of tetralogy of Fallot. American Heart Journal, 155, 182–186.

Thavendiranathan, P., Poulin, F., Lim, K. D., et al. (2014). Use of myocardial strain imaging by echocardiography for the early detection of cardiotoxicity in patients during and after cancer chemotherapy: A systematic review. Journal of the American College of Cardiology, 63, 2751–2768.

Therrien, J., Provost, Y., Merchant, N., et al. (2005). Optimal timing for pulmonary valve replacement in adults after tetralogy of Fallot repair. American Journal of Cardiology, 95, 779–782.

Thomas L, Marwick TH, Popescu BA et al (2019) Left atrial structure and function, and left ventricular diastolic dysfunction: JACC state-of-the-art review. J Am Coll Cardiol 73:1961–77. https://doi.org/10.1016/j.jacc.2019.01.059

Toro-Salazar, O. H., Gillan, E., O’Loughlin, M. T., et al. (2013). Occult cardiotoxicity in childhood cancer survivors exposed to anthracycline therapy. Circulation: Cardiovascular Imaging, 6, 873–880.

Tretter JT, Redington AN (2018) The forgotten ventricle? Circ. Cardiovasc. Imaging 11;3:e007410 https://doi.org/10.1161/CIRCIMAGING.117.007410.

Trusty, Phillip M, Timothy C Slesnick, Zhenglun Alan Wei, Jarek Rossignac, Kirk R Kanter, Mark A Fogel, and Ajit P Yoganathan. 2018. 'Fontan surgical planning: previous accomplishments, current challenges, and future directions', Journal of cardiovascular translational research, 11: 133-44.

Valente, A. M., Gauvreau, K., Assenza, G. E., et al. (2014). Contemporary predictors of death and sustained ventricular tachycardia in patients with repaired tetralogy of Fallot enrolled in the INDICATOR cohort. Heart, 100, 247–253.

Valverde, I., & Rojas, J. (2017). Personalized Three-Dimensional Printed Models in Congenital Heart Disease. Journal of Clinical Medicine, 8(4), 522.

van Bakel, Theodorus MJ, Kevin D Lau, Jennifer Hirsch-Romano, Santi Trimarchi, Adam L Dorfman, and C Alberto Figueroa. 2018. 'Patient-specific modeling of hemodynamics: supporting surgical planning in a Fontan circulation correction', Journal of cardiovascular translational research, 11: 145-55.

Van De Bruaene, A., Horlick, E. M., Benson, L., et al. (2019). Characterization of the surgically modified RVOT using magnetic resonance angiography in adults late after tetralogy of Fallot repair. Journal of the American College of Cardiology: Cardiovascular Imaging, 12, 1589–1591.

Van den Eynde J, Sá MPBO, Vervoort D et al (2022) Pulmonary Valve Replacement in Tetralogy of Fallot: An Updated Meta-Analysis. Ann Thorac Surg. 113:1036-1046. https://doi.org/10.1016/j.athoracsur.2020.11.040

van der Ven, J. P. G., van den Bosch, E., Bogers, A. J. C. C., & Helbing, W. A. (2018). State of the art of the Fontan strategy for treatment of univentricular heart disease. F1000Research, 7, F1000 Faculty Rev-935. https://doi.org/10.12688/f1000research.13792.1

Vliegen HW, van Straten A, de Roos A et al (2002) Magnetic resonance imaging to assess the hemodynamic effects of pulmonary valve replacement in adults late after repair of tetralogy of fallot. Circulation 106:1703-7 https://doi.org/10.1161/01.cir.0000030995.59403.f8.

Wald, R. M., Haber, I., Wald, R., et al. (2009). Effects of regional dysfunction and late gadolinium enhancement on global right ventricular function and exercise capacity in patients with repaired tetralogy of Fallot. Circulation, 119, 1370–1377.

Yoshida, M., Menon, P. G., Chrysostomou, et al. (2013). Total cavopulmonary connection in patients with apicocaval juxtaposition. European Journal of Cardio-Thoracic Surgery, 44(3), e46–e52.

Zablah, J. E., Misra, N., Gruber, D., et al. (2017). Comparison of patients undergoing surgical versus transcatheter pulmonary valve replacement: Criteria for referral and mid-term outcomes. Pediatric Cardiology, 38, 603–607.

Zhang, X., Alexander, R. V., Yuan, J., & Ding, Y. (2022). Computational Analysis of Cardiac Contractile Function. Current cardiology reports, 24(12), 1983–1994. https://doi.org/10.1007/s11886-022-01814-1

Zhuang B, Yu S, Feng Z, He F et al (2020) Left ventricular strain derived from cardiac magnetic resonance can predict outcomes of pulmonary valve replacement in patients with repaired tetralogy of Fallot Front Cardiovasc Med 18;9:917026 https://doi.org/ 10.3389/fcvm.2022.917026. eCollection 2022.